UiT The Arctic University of Norway

Faculty of Science and Technology
Department of Physics and Technology

Effects of subglacial meltwater runoff on the ocean circulation beneath the Filchner Ice Shelf

Johanne Jahnsen Hus

FYS-3900: Master's thesis in physics - 60 ECTS
June 2023

Abstract

Antarctic ice shelves, by restraining ice streams and affecting the discharge of grounded ice, play a critical role in the mass balance of the Antarctic ice sheet. In this study, sub-ice shelf CTD measurements and time series data from an ice shelf cavity mooring were used to detect subglacial runoff beneath the Filchner Ice Shelf. CTD measurements from four boreholes across the southern Filchner Ice Shelf show that subglacial runoff spreads along the shallower eastern and western flanks beneath the ice shelf. Analysis of the water mass properties at the easternmost borehole indicates that 32 % of the freshwater content in the upper mixed layer originates from subglacial runoff. It is hypothesized that the subglacial runoff observed at this site primarily originates from the Support Force Glacier, located approximately 182 km upstream of the drill sight. Between 2016 and 2022, six subglacial runoff events were detected by analysis of the time series data from the ice shelf cavity mooring. The subglacial runoff event shows a distinct pattern consisting of two phases. The first phase was identified through events of low source salinity, containing subglacial runoff. The events of low source salinity were followed by a rapid increase in source salinity, indicating phase 2 of the event. Anomalies of velocity, temperature, source salinity, and backscatter reveal that phase 2 of the subglacial runoff events result from a meltwaterladen ice shelf plume. These plumes, which are a result of the discharge of subglacial meltwater at the grounding line, are expected to contribute to increased basal melting in the deeper areas of the ice shelf. Analysis of current meter data shows that the meltwater plume modifies the mean current within the upper mixed layer. This is evident from increased velocities and a noticeable shift in the current direction. The sub-ice shelf data were used to approximate the subglacial runoff flux from the Support Force Glacier. From the CTD profile a subglacial flux of 5.7 $m^3 s^{-1}$ was derived. A time series of the subglacial runoff flux was developed based on the mooring data. This time series shows peaks in the subglacial runoff flux that coincide with the observed subglacial runoff event detected in source salinity. This indicates multimonth to interannual variability in the occurrence of the subglacial runoff events. This study is the first to derive a comprehensive runoff time series using under-ice shelf ocean moorings data. These findings expand on the knowledge of the overall circulation beneath the Filchner Ice Shelf and potential implications for future ice sheet stability.

Acknowledgements

What a year!! I have to start by thanking my fellow nerds, Elena and Julie. Thanks for the extra-long coffee breaks, late-night study sessions, and always keeping my spirits high.

A special shoutout to Mathilde for taking me on monthly "utekontor" adventures. You have kept me sane and given me an excuse to escape the four walls of my study cave.

Now, let's give a round of applause to my supervisor, Tore Hattermann, who has transformed into a living, breathing encyclopedia throughout the last year. Thank you for your guidance, patience and for sharing your enthusiasm for science. Also, thank you for the unforgettable cruise to Antarctica and the sailing trip around Cape Horn, which added an adventurous twist to my thesis journey.

"A thousand thanks" to Zoe, Lucas, and Elena, for generously lending your precious time on this planet to read over parts of my master's thesis.

A big thanks to Eric, my trusty support system. Thank you for being there, nodding as if my thesis ramblings were the most profound revelations in the universe.

And last but not least, I have to thank Mr. Worldwide, Pitbull. His infectious beats and uplifting lyrics have been a constant source of motivation and inspiration on this one-year roller coaster ride, getting me through even the toughest of days. As Pitbull himself says,

> This is for everybody going through tough times
> Believe me, been there, done that
> But every day above ground is a great day, remember that
> Dalé
>
> —Pitbull aka Mr.World wide

Contents

List of Figures

List of Tables

List of Acronyms

AABW Antarctic Bottom Water

FRIS Filchner Ronne Ice Shelf

FIS Filchner Ice Shelf

HSSW High Salinity Shelf Water

ISW Ice Shelf Water

mWDW Modified Warm Deep Water

RIF Ronne Ice Front

RIS Ronne Ice Shelf

SFG Support Force Glacier

1

Introduction

Antarctic ice shelves, floating extensions of the Antarctic ice sheet, play an essential role in the mass balance of the Antarctic ice sheet (Paolo et al., 2015). This is because more than 80% of the grounded ice in Antarctica drains through its ice shelves (Pritchard et al., 2012). The ice sheet experiences mass gain through snowfall, while mass loss occurs through meltwater runoff and ice discharge into the ocean (Shepherd et al., 2018). The ice shelves restrain the ice streams that feed into the ice shelves (Schoof, 2007; Goldberg et al., 2009). Ice shelf thinning may reduce the buttressing to inland glaciers and the retreat of grounding lines toward land (Zeising et al., 2022). Consequently, the ice streams that feed into the shelves will experience acceleration and thinning, allowing more grounded ice to reach the ocean (Rignot et al., 2004), potentially contributing to global sea level rise (Oppenheimer, 1998). The reduction in ice shelf volume primarily occurs due to two factors: melting at the ice shelf base or calving at the ice front (Nicholls et al., 2009a). The former is driven by the heat transfer from the ocean beneath the ice shelf (Pickard and Emery, 1990), while the latter occurs at the ice front due to instabilities within the ice (Cheng et al., 2021). In recent decades, satellite observations show that ice-shelf volume loss is accelerating in Antarctica, mainly due to increased melting at the ice shelf base (Jenkins et al., 2018; Paolo et al., 2015; Adusumilli et al., 2020) (Fig.2.1). Studies by Paolo et al. (2015) show persistent volume loss has been observed in West Antarctica since 1994 due to increased basal melt. Furthermore, the study reveals that from 2003 to 2013, the ice shelves in East Antarctica also experienced a moderate level of ice loss due to basal melting. Increased basal melting does not only impact the ability of ice shelves

to buttress inland glaciers but will also have implications for the formation of Antarctic Bottom Water (AABW), a dense water mass that plays a key role in global ocean circulation (Orsi et al., 1999).

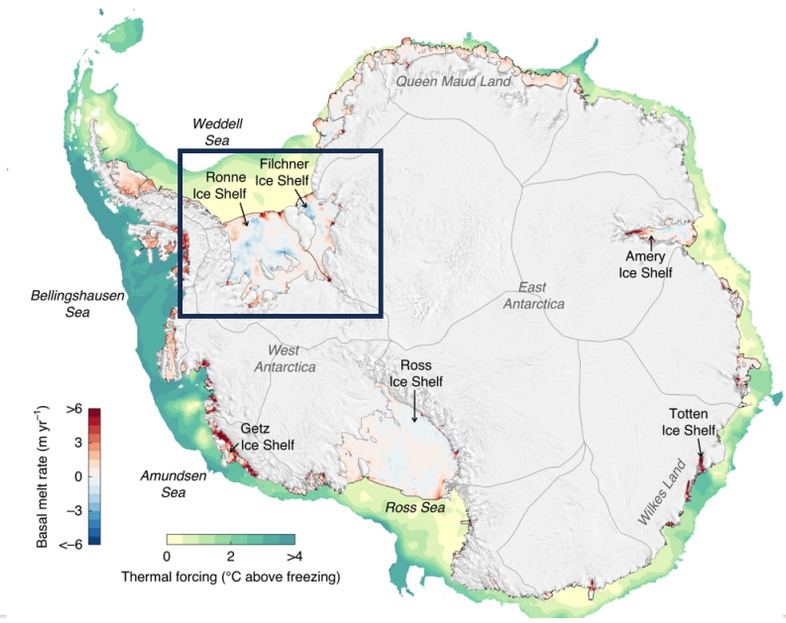

Figure 1.1: Basal melt rates averaged from 2010-2018 of Antarctic ice shelves. The study area of this thesis, FRIS, is marked with a square (Adusumilli et al., 2020)

The generation of meltwater at the ocean-ice interface is typically considered the primary source of buoyancy, driving the stratification of the water column and overturning circulation within the sub-ice shelf cavity. Jenkins (2011) used plume modeling to demonstrate how buoyancy resulting from subglacial discharge within an ice shelf cavity can serve as a triggering mechanism that enhances basal melting in proximity to the grounding line. When lighter freshwater from subglacial discharge enters the ice shelf cavity, it creates a buoyancy force, initializing a rising plume of freshwater (Motyka et al., 2003). This plume entrains warmer ambient water, which causes melting of the ice shelf base and an increase of the plume's volume (Jenkins, 2011). As the plume ascends along the ice base, it will start generating shear-driven turbulence, further enhancing the entrainment of warmer water from the underlying layers (Nicholls et al., 2009a). The process of entrainment transfers salt, heat, and momentum between a turbulent layer and a non-turbulent layer, normally occurring due to shear at their interface (Durst et al., 2012). The enhanced melting caused by the plume can create a basal meltwater channel in the ice shelf base (Drews, 2015).

The Filchner-Ronne Ice Shelf (FRIS) is the largest ice shelf by volume in Antarctica, and it drains both West and East Antarctic ice sheets (Joughin and Vaughan, 2004) (Fig.2.1). On the eastern side of FRIS lays the Filchener Ice Shelf (FIS), and the study area of this thesis is the ice shelf ocean cavity beneath FIS. At FIS, the ice stream known as the Support Force Glacier (SFG) feeds into the ice shelf (Hofstede et al., 2021a). Model findings by Dow et al. (2022) indicate that subglacial runoff flows into FIS at the grounding line through subglacial channels within SFG, draining two small channels with a subglacial discharge of 0.51 and 0.45 $m^3\ s^{-1}$. Subglacial runoff has also been detected at the eastern flanks of FIS by Huhn et al. (2018), which used noble gas samples of helium to detect subglacial runoff. The results indicated that 13% of the freshwater content on the eastern flank below FIS could be traced to subglacial runoff. Hofstede et al. (2021b) used seismic profiles to identify a basal meltwater channel within the ice shelf base of FIS. This basal meltwater channel was found to extend from the grounding line of SFG and 7.7 km upstream, with a grounding line fan located at the same point. These findings imply that subglacial discharge occurs at the grounding line of SFG, and that this runoff contributes to basal melting, leading to the formation of the meltwater channel within the ice shelf base of FIS.

Although some existing models have investigated the plume-driven melting process resulting from subglacial runoff, the understanding of how subglacial runoff influences the circulation beneath FIS remains incomplete due to the limited availability of observational data. Hence, the main objective of this thesis is to enhance our understanding of the impacts of subglacial runoff on the circulation and basal melting processes beneath the FIS. This thesis is based on the hypothesis that subglacial runoff enters the ice shelf cavity at the grounding line of the Support Force Glacier (SFG) and subsequently spreads along the eastern flanks of FIS. The analysis and interpretation of Conductivity, Temperature, and Depth (CTD) measurements from 2016 are utilized in this study, focusing on four boreholes situated beneath the relatively shallower eastern and western flanks of FIS. Additionally, the analysis includes time series data from an ice shelf cavity mooring covering the period from January 2016 to December 2022 from the eastern flank. The thesis follows a three-step approach: firstly, detecting subglacial runoff beneath FIS from the CTD measurements and the mooring time series. This is done by investigating the fraction of subglacial runoff in the CTD profiles' upper layers and identifying specific subglacial runoff events within the time series data. This step is important to quantify the presence of subglacial runoff beneath the ice shelf. Secondly, once the subglacial runoff events are detected, the subglacial runoff event influence on the ocean circulation beneath FIS is examined. This investigation aims to understand how these runoff events affect the flow patterns and dynamics of the ocean currents in the region. In the final stage of the study, a time series of the subglacial runoff flux is derived from the mooring data to investigate the magnitude and variability

of the subglacial runoff. The findings of this thesis provide insights into the impact of subglacial runoff on the circulation beneath FIS and the dynamics of ice-ocean interactions beneath FRIS. These insights deepen our understanding of the processes and characteristics of the formation of a buoyant plume that is triggered when subglacial runoff is discharged at the grounding line. Additionally, it can provide insight into the implications for the future behavior of the Antarctic ice sheet.

1.1 Thesis Outline

In this thesis, the following structure is adopted to present the research findings:

- **Section 2: Background:** Overview of geographical and oceanographic settings relevant to the study area, including key features of FRIS, factors driving circulation beneath the ice shelf, subglacial runoff theory, and its impact on ocean circulation. Additionally, essential oceanographic concepts are incorporated to understand the observed dynamics in the results.

- **Section 3: Method:** Description of the CTD and mooring instruments used for data collection. The deployment locations of the instruments and the drilling site for accessing subglacial environments are specified. The data processing steps, including calibration and correction procedures, are explained. The derivation of source salinity, freshwater fraction, and subglacial runoff flux estimations are detailed, including the mathematical formulas.

- **Section 4: Results:** Presentation of the findings obtained from the analysis. This includes the detection of subglacial runoff, time series data from the mooring sites, showcasing variations in oceanographic parameters such as temperature, salinity, and current velocities. Anomalies in these parameters are examined and linked to subglacial runoff. Additionally, a subglacial runoff model is developed and compared with the observed data, providing insights into the dynamics and magnitude of the runoff flux.

- **Section 5: Discussion:** Interpretation and analysis of the results in the context of subglacial runoff flux, the characteristics of an Ice Shelf Plume initiated by subglacial runoff, and the effects this will have on the residual current. The implications of these findings on ice sheet stability and future climate scenarios are discussed.

- **Section 6: Summary:** Summarization of the main findings from the analysis and the study's contributions to the field are highlighted. Finally, areas for future research are suggested to expand knowledge in this area further.

2

Background: Geographical and Oceanographic Setting

2.1 Geographic Setting

Ice shelves are created when the ice at the oceanic boundary of an ice sheet does not break off into icebergs at the grounding line but instead remains connected to the grounded ice sheet as a floating extension (Nicholls et al., 2009a). The grounding line represents the transition point where an outlet glacier transitions from resting on bedrock to floating over a body of water (Paolo et al., 2015). The ice in an ice shelf has two possible outcomes: it can either break off as icebergs from the edge facing the sea, known as the ice front, or it can melt from the ice shelf's base due to heat transfer from the ocean (Nicholls et al., 2009a). According to research conducted by Depoorter et al. (2013), with the use of satellite radar altimeter measurements and ice-penetrating radar (IPR) data, the mass loss of Antarctica as a whole is approximately equally distributed between basal melt loss and calving. Upon closer analysis of FRIS, it was found that the primary reason for the mass loss is calving at the ice front, accounting for approximately 83% of the total loss. The remaining 17% is attributed to basal melt (Depoorter et al., 2013).

Located in the southern Weddell Sea, FRIS is the largest Antarctic ice shelf in terms of ice volume (Nicholls et al., 2009a) (Fig.2.1). It covers an area of 450,000 km^2 (Nicholls et al., 2004) and has an average ice thickness of 700 m

(Lambrecht et al., 2007). The southern Weddell Sea has a distinct topographic feature where the continental shelf gradually deepens towards the grounding line (Nicholls et al., 2004). Beneath FIS, a deep trough known as the Filchner Trough extends over the continental shelf and intersects with the shelf break to create the Filchner Sill (Nicholls et al., 2009a). At the grounding line, the Filchner Trough reaches its maximum depth of 1800 m, making it the deepest point of FRIS. The Ronne Ice Shelf (RIS) is located on the western side of FRIS Nicholls et al. (2009a). Below the RIS lies the Ronne Depression, a geographical feature smaller than the Filchner Trough, which only stretches a short distance north of the ice front. Berkner Island is an Antarctic ice rise between FIS and RIS (Nicholls et al., 2001). Ice rises are formed when ice shelves are grounded on an elevated seabed, resulting in small-scale topographic features. The flowing ice shelf is redirected around the grounded region, creating a characteristic dome-shaped ice sheet (Matsuoka et al., 2015).

Three major ice streams, known as the Foundation Ice Stream, the Support Force Glacier, and the Recovery Ice Stream, contribute to the ice flow into FIS (Jezek, 1999). Ice streams are high-velocity corridors within an ice sheet that transport large volumes of ice from the continent's interior toward the ice shelf (Bennett, 2003). The flow of the ice streams is primarily governed by gravitational forces, specifically the downward weight of the ice mass, which depends on the slope of the ice surface and its thickness (Paterson, 1981). This thesis specifically focuses on the SFG, located on the southeastern side of FIS. The grounding line of SFG reaches a depth of approximately 1300 m (Norsk Polarinstitutt, 2023)

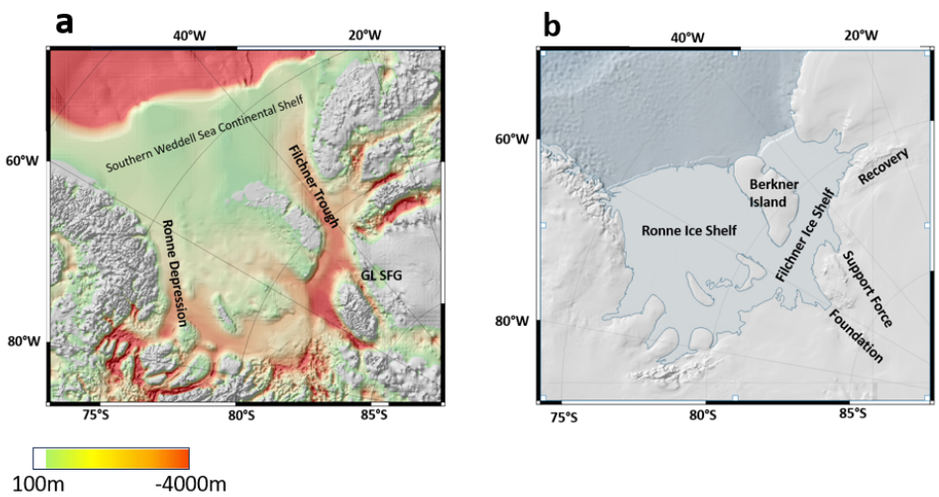

Figure 2.1: Panel (a) shows a map of the seabed beneath the Filchner Ronne Ice Shelf. The grounding line of the Support Force Glacier is marked with GL SFG. Panel (b) map of the Filchner Ronne Ice Shelf and Ice stream feeding into the Filchner Ice Shelf. The maps are constructed with Quantartica (Norsk Polarinstitutt, 2023)

2.2 Processes within the ice shelf cavity

2.2.1 Circulation Beneath the Filchner-Ronne Ice Shelf

Several factors, including thermohaline processes, ice shelf-ocean interactions, and tides, influence the ocean circulation beneath FRIS (Makinson and Nicholls, 1999). The ocean is shielded from atmospheric forcing by the layer of ice covering it. The main driver of the residual current beneath FRIS is the east-west density gradient caused by a combination of dense modified Warm Deep Water (mWDW) on the continental shelf in front of RIF and less dense modified water masses within the ice shelf cavity (Nicholls et al., 2009a). The term "residual current" is used to describe the combined effect of the background current and its associated anomalies.

High Salinity Shelf Water (HSSW) is created in an open water area within the sea ice, called a latent heat polynya (Nicholls et al., 2009b). The polynya is located northwest of the RIF (Haid and Timmermann, 2013) and is sustained by katabatic winds and tides. The polynya allows for large heat loss to the atmosphere, facilitating sea ice formation. When sea ice forms, brine is released, which causes an increase in salinity. The brine rejection mixes with the mWDW on the continental shelf, resulting in Ronne-HSSW (Nicholls et al., 2009a).

In polar regions, the salinity of seawater is the primary factor determining the density (Nicholls et al., 2004). HSSW, with a surface-freezing temperature ($\sim$ -1.9 $^{\circ}C$) and practical salinity S>34.62 psu (Orsi and Wiederwohl, 2009), is denser than surrounding water masses, leading to vertical mixing and convection (Nicholls et al., 2009a). HSSW either descends the continental shelf, contributing to a bottom water formation or is left as dense water on the shelf. Because the continental slope deepens towards the grounding line, the dense water can sink southward down the slope and eventually enter the sub-ice shelf cavity (Nicholls et al., 2001). Observations suggest that HSSW enters the sub-ice cavity via the Ronne Ice Front (RIF) (Nicholls et al. (2004, 2001)). The HSSW inflow at RIF leads to a thermohaline circulation beneath the ice shelf, generating the background current within the ice shelf cavity (Janout et al., 2021). The HSSW inflow follows two main pathways: one branch flows into the Ronne Depression, while the other heads east, reaches the west coast of Berkner Island, and rounds the southern tip entering the deeper parts of the ice shelf cavity (Nicholls et al., 2009a). In the deep parts of the sub-ice shelf cavity, HSSW can melt the ice shelf from below, where the pressure effect lowers the freezing point by $0.75^{\circ}C$ for every kilometer of water depth (Millero, 1978; Fofonoff and Millard Jr, 1983). The HSSW is converted to Ice Shelf Water (ISW) by mixing with the meltwater. ISW is a less saline and colder water mass, characterized by below-surface freezing temperatures (<1.9 °C) (Nicholls et al., 2009a). The ISW then emerges at the FIS cavity via the Filchner Trough.

According to Hattermann et al. (2021), two distinct modes are driving the background circulation beneath FRIS: the Ronne mode and the Berkner mode (Fig.2.2). These modes vary on an interannual timescale and are determined by the magnitude of Ronne-HSSW forming during winter. In the Ronne mode, the Ronne-HSSW serves as the main driver of the background circulation that spans the entire FRIS cavity (Fig. 2.2b). Conversely, during periods of the Berkner mode, the production of Ronne-HSSW is reduced, allowing a less saline Berkner-HSSW, generated north of Berkner Island, to penetrate the ice front of FIS and circulate within the northern section of the Filchner Trough (Hattermann et al., 2021) (Fig. 2.2a).

Strong spring tides beneath FRIS have been documented through observations and model findings (Nicholls et al., 2009a). Additionally, Hattermann et al. (2021) observed strong tidal currents beneath FIS, with velocities often exceeding 50 cm s^{-1} during spring tides on the eastern and western flanks. The tidal currents beneath the ice shelf can influence the thermohaline circulation by inducing vertical mixing (MacAyeal, 1984). The tidal oscillation also contributes to heat and salt transportation beneath the ice shelf (Makinson and Nicholls, 1999).

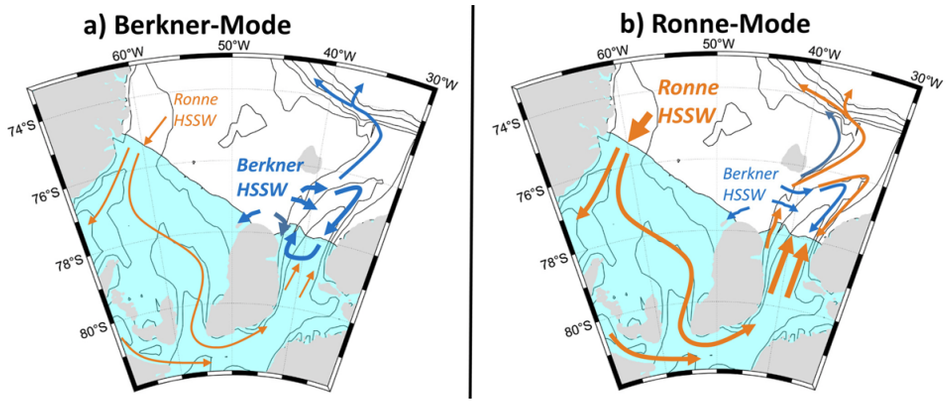

Figure 2.2: Panel (a) map illustrating the background current during the Berkner mode, characterized by the inflow of Berkner HSSW into the Filchner Ice Front. Panel (b) showcases the residual current during the Ronne mode, where Ronne-HSSW dominates in the circulation beneath FRIS. Illustration extracted from Janout et al. (2021)

.

2.2.2 Basal Melt and Ice Shelf Water Plumes

In this thesis, the phase change from ice to liquid at the ice shelf-ocean interface is referred to as basal melt or melting. However, the phase change is primarily attributed to the ablation of the ice shelf base caused by a transfer of heat and salt from the surrounding seawater to the ocean-ice interface (Malyarenko et al., 2020). The amount of turbulence found in the water column and the temperature and salinity gradient across the boundary layer are the determining factors for ablation (Nicholls et al., 2009b). Ablation occurs through two thermal regimes, either dissolving or melting (Kerr, 1994; Kerr and McConnochie, 2015; Woods, 1992). In Malyarenko et al. (2020), two examples of the different ablation scenarios are described. Firstly, when a glacier terminates in the water, it melts if the water temperature is warm enough to bring the interface to the melting-point temperature of pure water (0 °C at surface pressure). In this scenario, melting occurs as heat is transferred from the surrounding ocean to the ocean-ice interface. In the case of an ice shelf-ocean interface located 1000 meters below sea level, melting can not occur if the surrounding ocean is colder than -0.75 °C (the in-situ freezing point of freshwater at 1000m depth). Instead, a phase change may occur due to dissolving if a salt flux is transported to the ocean-ice interface. Dissolving occurs due to the relationship between salinity and the freezing point temperature: as salinity increases, the freezing point temperature decreases. Consequently, the presence of a salt flux can effectively lower the local freezing point, enabling the occurrence of a phase change.

The production of ISW caused by the formation of a buoyant plume is seen in

Fig.2.3. When dense HSSW enters the ice shelf cavity and reaches the deepest parts of the ice shelf, the freezing point temperature is lowered sufficiently enough for melting to occur due to pressure effects (Nicholls et al., 2009a). When the basal ice melts, it creates a layer of less dense meltwater which mixes with HSSW to form ISW. The density difference between the ISW and the surrounding seawater generates a buoyancy force that causes the ISW to rise along the sloping ice shelf base, forming a plume that preferably flows towards the thinnest areas of the ice shelf. As it ascends along the ice shelf base, the ISW entrains warmer, more saline water from below, which causes further melting of the ice shelf base. As the plume rises, this process continues. Consequently, the volume flux of the plume increases with height (Jenkins, 2011; Nicholls et al., 2009a). When the ice shelf base is relatively smooth, the friction coefficient is small. As a result, if the buoyant plume grows in size and its velocity increases significantly, it can transition toward a state of near-geostrophy. Within this near-geostrophic regime, the plume aligns itself with constant topographic contours, representing the height of the water column (Holland and Feltham, 2006). The rising plume's freezing point temperature increases as the pressure decreases, which can cause supercooling and potential refreezing of the ISW plume, forming marine ice at the ice shelf base (Nicholls et al., 2009a). Also, The heat required for ice melting is primarily derived from the ocean thus, the ocean water can experience a cooling effect as it transfers its heat energy to melt the ice (Gade, 1979).

Observational analyses are expected to reveal specific characteristics of the ISW plume. Based on the theory of the ISW plume, it is anticipated that the ISW plume will exhibit anomalies from the background current, showing northward anomalies that can be identified by two key features: colder water, indicative of a cooling effect, and higher source salinity resulting from the entrainment of more saline water from the lower layers in the ice shelf cavity.

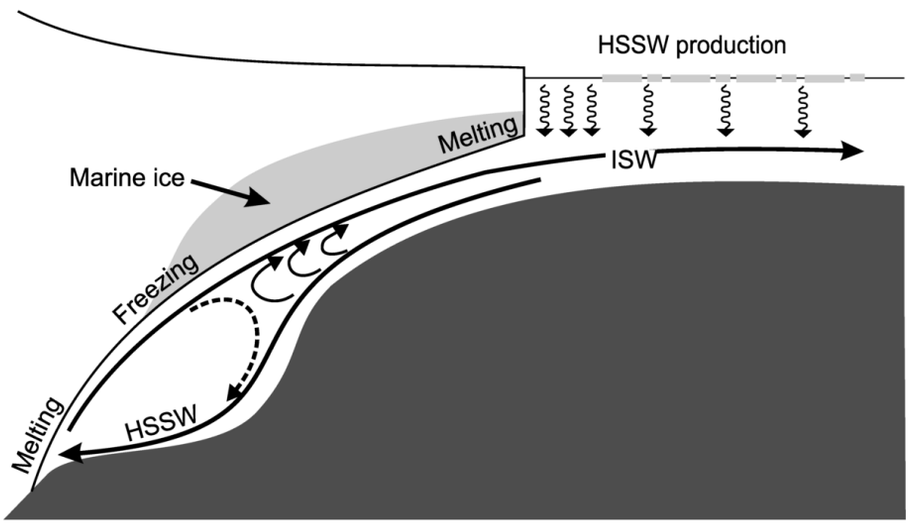

Figure 2.3: Illustration of an ISW plume forming beneath FRIS, showing the process of melting and freezing. Illustration extracted from Nicholls et al. (2009a).

2.2.3 Gade Line

When HSSW with temperatures higher than the in-situ freezing point, comes into contact with the base of an ice shelf, it leads to the melting of the ice. This, in turn, causes the water column to become fresher (Nicholls et al., 2009b). The freshening of the water column gives rise to a linear trajectory of the water mass properties in a temperature-salinity space, passing through the source water (S_0, T_0), with a gradient given by Gade (1979):

$$\frac{d\theta}{dS} = \underbrace{\frac{L}{S_0 c_w}}_{(1)} + \underbrace{\frac{(\theta_f - T_i)c_i}{S_0 c_w}}_{(2)} + \underbrace{\frac{\theta_0 - \theta_f}{S_0}}_{(3)} \tag{2.1}$$

Where θ_f is the potential temperature at which ice melts at the ice shelf base, T_i is the temperature of the core of the ice shelf; c_i and c_w are the specific heat capacities of ice and water (around 2010 J kg^{-1} ^{o}C^{-1} and 4000 J kg$^{-1}{}^o$C^{-1}), L is the latent heat of fusion of ice ($3.35 * 10^5$ Jkg^{-1}), and S_0 is the source water mass salinity ($S_0 > 34.62$ for HSSW). In Eq.2.1, the first term on the right-hand side (~ 2.4) is dominating and explains how much heat is needed to melt a certain amount of ice; The second term only applies to melting regimes and approximates the heat needed to warm the ice to freezing temperature; the third term accounts for the need to cool the seawater to the freezing point (Nicholls et al., 2009b). Aligning data points with the Gade-line in a T-S space can indicate the presence of freshwater from basal melting.

When computing the Gade line for temperatures (T_i > -30° C) appropriate to FIS (Nicholls et al., 2009b) and when the volume of meltwater is small relative to the ocean volume, terms two and three in Eq.2.1 are neglected by assuming that latent heat transfer from the ocean to ice exceeds the sensible heat transfer from the ocean to ice, hence neglecting the melting term (Wåhlin et al., 2010). The third term, water cooling, is small relative to latent heat transfer and is insignificant (Nicholls et al., 2009b). The temperature and salinity of the ocean-meltwater mixture will be expressed as follows:

$$T_1(S_1) = \frac{L}{c_w}(\frac{S_1}{S_0} - 1) + T_0 \tag{2.2}$$

$$S_1(T_1) = S_0(1 - \frac{c_w}{L}(T_0 - T_1)) \tag{2.3}$$

Where T_1 and S_1 are temperature and salinity resulting from meltwater mixing. T_0 and S_0 are the temperature and salinity of the source water mass.

2.3 Subglacial Channels and Discharge

The Antarctic Ice Sheet is polythermal (Greve and Blatter, 2016), meaning the ice sheet consists of glaciers with different thermal regimes (Knight, 1999). The glaciers are primarily characterized by cold temperatures due to the cold climate, with a temperate layer at their base (Greve and Blatter, 2016), causing a temperature gradient from the glacier base to the glacier surface. The melting point of the glacier ice is affected by the weight of the ice mass above it (0°C at atmospheric pressure), where the pressure-dependent melting point decreases by 0.0073 °C per bar of pressure within the glacier (Hagg, 2022). According to Pattyn (2010), approximately 55% of the grounded ice of the Antarctic ice sheet experiences pressure melting. This includes areas such as ice streams and regions underlain by subglacial lakes (Stokes and Clark, 1999; Wright and Siegert, 2012). When the ice flows over the bedrock, the friction between the ice and the underlying bed generates heat, which can melt the glacier base and form subglacial meltwater (Knight, 1999). The magnitude of the frictional heat is directly related to both the sliding velocity and the basal shear stress (Thøgersen et al., 2019). In addition to friction-generated heat, subglacial meltwater can arise from the geothermal heat flux (Knight, 1999). This heat flux originates from the Earth's interior and contributes to raising the temperature of the glacier bed, leading to the melting of the glacier from below. When the glacier base is below the melting point, the subglacial basal melt is primarily generated through frictional heating and geothermal heat fluxes. However, as the bed approaches the melting point, the temperature at the glacier base is

also influenced by the release of latent heat from melting ice or absorbing latent heat during freezing (Knight, 1999).

The movement of subglacial meltwater is mainly determined by hydraulic potential, which drives subglacial meltwater originating in high-pressure zones to flow along the glacier bed towards regions of lower pressure (Knight, 1999). The height of the ice surface controls the pressure and influences the direction and dynamics of subglacial meltwater flow (Alley (2011); Fountain and Walder (1998)). Typically, this leads to the subglacial meltwater following the same pathways as the ice, flowing from the ice sheet's interior toward the grounding line. When the water flows downstream, it transports sediment from the underlying bedrock, leading to erosion of the glacier base. Moreover, the flowing meltwater contains sensible heat that can be transferred to the glacier base, which can enlarge subglacial channels within the glacier base (Shroder et al., 2021). Channels within the glacier base are often called Röthlisberger channels (R-channels). Channels may also develop within the subglacial sediment bedrock, referred to as Nye-Channels (Knight, 1999). The subglacial meltwater will eventually be discharged at the grounding line into the ice shelf ocean cavity. At this point, the subglacial meltwater typically exhibits zero salinity and a temperature corresponding to the pressure-dependent melting point of freshwater. Upon discharge at the grounding line, the subglacial runoff undergoes a buoyancy-driven ascent, driving convective-driven melting close to the grounding line (Motyka et al., 2003). This upward movement results from the low density of the subglacial runoff relative to the surrounding water within the ice shelf cavity. Once the subglacial runoff initiates upward movement, it will gradually entrain the warmer and more saline HSSW, initiating basal melting. According to the findings presented by Jenkins (2011), the melting rate in the immediate downstream region of the grounding line exhibits a direct relationship with the cube root of the freshwater flux. This indicates that a change in flux by approximately an order of magnitude doubles the melt rates. Thus the subglacial runoff can potentially act as a triggering mechanism for forming an ISW plume. As the plume rises, it will generate shear, entraining more of the ambient ocean. This process enhances both the melt rates and the buoyancy of the plume. Consequently, the importance of the subglacial runoff flux on the melt rate diminishes as the initial flux gradually becomes less important in determining the overall buoyancy of the plume (Jenkins, 2011). Subsequently, the ISW plume will ascend as illustrated in Fig.2.3. The transition from convection-driven melting to shear-driven melting occurs smoothly, enabling a gradual and uninterrupted transition between these two regimes (Jenkins, 2011).

Estimating the magnitude of subglacial discharge at the grounding line is challenging due to the difficulty in obtaining direct measurements. In Antarctica, glacial basal melting primarily drives subglacial discharge, making seasonal discharge unlikely (Dow et al., 2018). There are instances where meltwater

accumulates in subglacial lakes (Siegert et al., 2005), typically forming where there is a depression in the bedrock topography (Tabacco et al., 2006). Subglacial lake growth and drainage are driven by the change in hydraulic potential within the ice stream (Dow et al., 2018). When the pressure within the subglacial lake reaches a threshold, it can trigger drainage through subglacial channels (Dow et al., 2016). Eventually, the drainage from the subglacial lakes will reach the grounding line, leading to a greater discharge of subglacial runoff into the ice shelf cavity(Dow et al., 2022). Subglacial lakes can take months to years to fill and drain, and the process is often unsteady and characterized by unpredictable episodic discharge events (Fricker et al., 2007; Stearns et al., 2008). Subglacial lakes have been identified upstream of the SFG with Land Elevation Satellite (ICESat) (Fricker et al., 2016). The presence of these subglacial lakes raises the anticipation of increased subglacial runoff drainage at the SFG due to potential lake drainage events. The glacial meltwater carries substantial amounts of glacially-eroded sediment that are deposited near the grounding line (Powell, 1990; Drews et al., 2017). Suspended sediment in the meltwater can also be a useful indicator for identifying buoyant plumes induced by subglacial runoff (Schild et al., 2016). In contrast with Antarctica, Arctic Greenland subglacial channels are dominated by surface meltwater, resulting in a strong seasonal cycle (Chandler et al., 2013; Washam et al., 2019).

2.4 Oceanographic Concepts

2.4.1 Geostrophic Currents and Thermal Wind Relation

A geostrophic current is an oceanic current characterized by the balance between the Coriolis force and the pressure gradient force (Pickard and Emery, 1990). An equilibrium state is achieved in the free ocean when boundary layer friction is negligible and the Rossby number is much less than one. In this state, the Coriolis force is the dominant driving force for large-scale flows, and inertial effects can be neglected (Klinger and Haine, 2019). The geostrophic balance results in a current flow parallel to the isobars (lines of constant pressure). In the Southern Hemisphere, the current flow is to the right of high pressure. Differences in mass distribution determine the horizontal pressure gradient in the ocean. This occurs due to two main factors. Firstly, variations in sea-surface height create sloping profiles where there is an accumulation of water in certain areas compared to others. This occurs in barotropic conditions, where surfaces of constant pressure and density are parallel. Secondly, horizontal density gradients contribute to mass distribution, with regions of denser water exhibiting higher mass and, consequently, higher pressure (Pickard and Emery, 1990). This is particularly relevant in baroclinic fluids, where the isobars are

inclined relative to the isopycnals (lines of constant density). Thus, the pressure component of the geostrophic current in the ocean can be decomposed into two terms: a barotropic term and a baroclinic term. The decomposition is derived from the hydrostatic balance equation, $\frac{\partial P}{\partial z} = -\rho g$, which describes the equilibrium between the vertical component of the pressure gradient force ($\frac{1}{\rho}\frac{\partial P}{\partial z}$) and the gravitational acceleration (g) (Talley, 2011). The geostrophic balance in the ocean can thus be expressed as :

$$fv = \frac{1}{\rho_0}\frac{\partial P}{\partial x} = \overbrace{g\frac{\partial \eta}{\partial x}}^{\text{barotropic}} - \overbrace{\frac{g}{\rho_0}\int_z^{\eta}\frac{\partial \rho}{\partial x}\,\partial z}^{\text{baroclinic}} \tag{2.4a}$$

$$fu = -\frac{1}{\rho_0}\frac{\partial P}{\partial y} = -\overbrace{g\frac{\partial \eta}{\partial y}}^{\text{barotropic}} + \overbrace{\frac{g}{\rho_0}\int_z^{\eta}\frac{\partial \rho}{\partial y}\,\partial z}^{\text{baroclinic}} \tag{2.4b}$$

Where f is the Coriolis parameter ($2\omega \sin\theta$), v (positive northward) and u (positive eastward) are velocity vector components, $\frac{\partial P}{\partial y}$ and $\frac{\partial P}{\partial x}$ is the horizontal pressure gradient in x and y direction, η is the displaced sea surface height, g is the gravitational constant (9.81 m s^{-1}), $\frac{\partial \rho}{\partial y}$ and $\frac{\partial \rho}{\partial x}$ represent horizontal density gradient in x and y direction, z is the water column depth, ρ_0 is the reference density applied with the Boussinesq approximation, assuming that the ocean is incompressible the density remains constant despite any variations in pressure (except in the hydrostatic equation) (Talley, 2011).

The thermal wind expresses the relationship between a vertical velocity shear in a horizontal geostrophic current and the horizontal density gradients (Klinger and Haine, 2019). The thermal wind relation is only relevant in baroclinic fluids because the misalignment of isolines causes the pressure gradient force to change with depth. Therefore, the geostrophic current will also vary with depth. A barotropic fluid has no vertical shear because the isobars and the isopycnals align. Consequently, the flow remains unaffected by variations in depth within the water column (Talley, 2011). The thermal wind relation can be derived in terms of the baroclinic geostrophic balance term:

$$f\frac{\partial v}{\partial z} = -\frac{g}{\rho_0}\frac{\partial \rho}{\partial x} \tag{2.5a}$$

$$f\frac{\partial u}{\partial z} = \frac{g}{\rho_0}\frac{\partial \rho}{\partial y} \tag{2.5b}$$

In the Southern Hemisphere, denser water is situated to the right of the thermal wind, while lighter water is positioned to the left. Fig.2.4 shows an example of a vertical velocity shear caused by horizontal density differences in a stratified fluid. Lighter water is found to the right (East) of the geostrophic current ($\rho_3 > \rho_2 > \rho_1$) ($\frac{\partial \rho}{\partial x} < 0$), there is no sea surface slope (barotropic conditions

negligible) and f < 0 on the Southern hemisphere. These conditions result in a geostrophic baroclinic current in the northward direction, decreasing from the bottom toward the sea surface ($\frac{\partial v}{\partial x} < 0$).

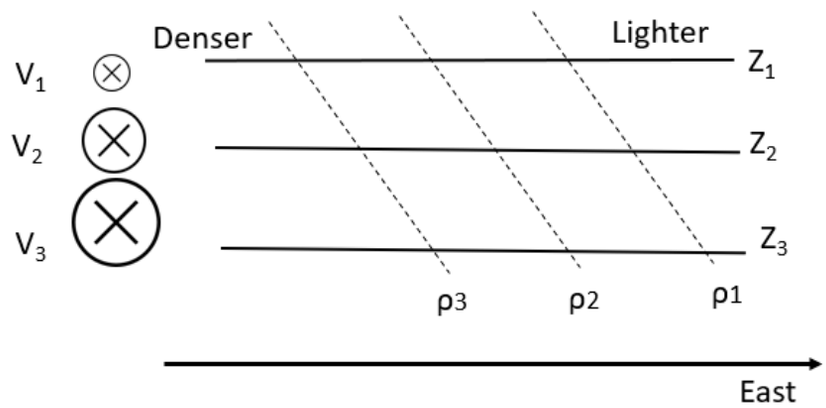

Figure 2.4: A scenario of vertical velocity shear in a baroclinic geostrophic current in the Southern Hemisphere. Lighter water is situated to the right (east) while dense water is situated to the left (west) ($\rho_3 > \rho_2 > \rho_1$) decreasing from the bottom. Z represents the depth where $z_3 > z_2 > z_1$. The ocean current flows toward the north and decreases towards the surface.

3

Method

3.1 Filchner Ice Shelf CTD and Mooring Stations

The data studied in this project were obtained from four sub-ice shelf conductivity, temperature, and depth (CTD) measurements and one ice shelf cavity mooring stationed on FIS between Berkner Island and the mainland. The CTD measurements and mooring deployment were conducted collaboratively by the Alfred Wegener Institute and the British Antarctic Survey in late December 2015 and early January 2016. The mooring's observations extended until 2022, providing valuable long-term data on the studied region (Alfred Wegener Institute, 2023).

An SBE 49 fast-cat CTD was used to collect data at the four stations located on the western and eastern flank of FIS. The stations, namely FSW1, FSW2, FSE1, and FSE2 are listed in Tab. 3.1, while Fig.3.1a provides a visual representation of their geographical locations within the study area.

Table 3.1: Field Sites, geographical coordinates, date of casts, amount of casts, and ice shelf thickness from each field site.

Field Site	Latitude	Longitude	Date of cast	Amount of casts	Ice thickness
FSW1	80.43°S	44.43°W	December 27th, 2015	1	853m
FSW2	80.48°S	44.18°W	January 20th, 2016	3	872m
FSE1	80.97°S	41.44°W	January 11th, 2016	2	891m
FSE2	81.07°S	40.82°W	January 4th, 2016	4	837m

The location of the ice shelf cavity mooring studied in this project was in the same position as the FSE2 CTD profile. The FSE2 mooring was deployed on January 6th, 2016, and has available data until December 30th, 2022. The mooring was equipped with six Seabird SBE37 MicroCATs, measuring conductivity, temperature, and depth of the seawater every second hour. The MicroCATs were located at 750m, 840m, 930m, 1006m, 1080, and 115m depths. Four Nortek Aquadopp acoustic current meters (ADCP), measuring current velocity and back-scatter every second hour, were attached alongside the two upper and lower MicroCATs. The ADCP data is only available until July 2020. The mooring is not possible to recover but is transmitting data to a data logger at the ice shelf's surface. A drawing of the mooring setup can be seen in Fig.3.1b. The measurements are used to study the temperature, salinity, backscatter, and velocity distribution beneath the ice shelf and to understand how these properties vary with depth and time.

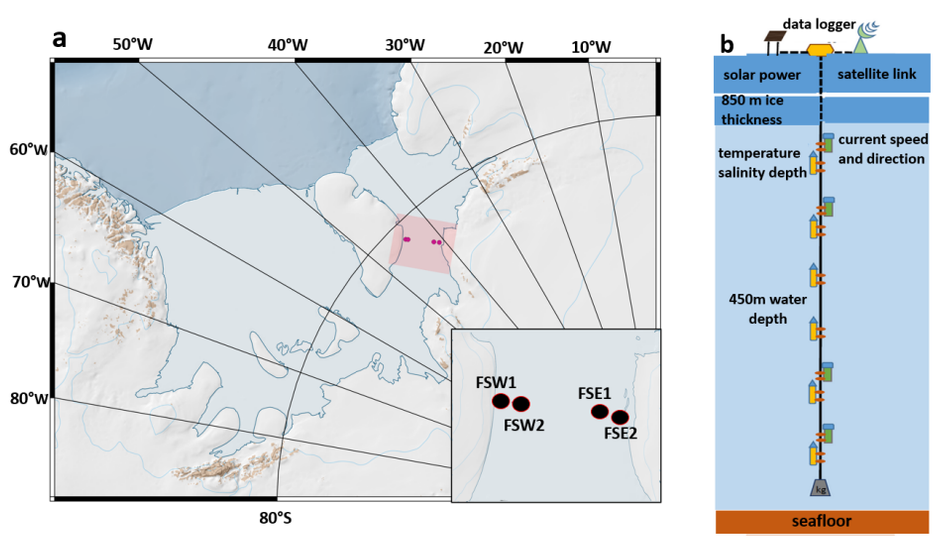

Figure 3.1: Panel (a) shows the position of the field sites FSW1, FSW2, FSE1 and FSE2, and the mooring position at FSE2 on FIS. Panel (b) shows the sub-ice shelf mooring setup on FIS. Attached to the mooring are six Seabird SBE37 MicroCATs (at 1150 m, 1080 m, 1006 m, 930 m, 840 m, and 750 m) and four Nortek Aquadopp acoustic current meters (at 1150 m, 1080 m, 840 m, and 750 m). Graphic by Alfred Wegener Institute (2023).

3.1.1 Calibration and Data Processing

The CTD measurements were calibrated and processed by Hattermann et al. (2021). Initially, the measurements were grouped into a common vertical grid. Subsequently, the average of the measurements from each station was com-

puted, resulting in a single CTD profile for each station.

To account for the challenges posed by the inability to recover the mooring and potential instrument drift, post-calibration of the MicroCAT data was carried out following the CTD profile at FSE2. This approach allowed for adjustments and calibration of the MicroCAT measurements to ensure accuracy and reliability. When the mooring was deployed, measurements were conducted every 10 seconds for the first hour. The calibration was done by calculating the mean temperature and conductivity for the first 30 minutes of all six MicroCAT instruments. Then the difference between the means and the temperature and conductivity at the corresponding depths in the CTD profile was determined. Further, the offset was subtracted from the MicroCAT raw data. A temperature-conductivity space displaying the calibration is seen in Fig.3.2.

Before smoothing the data, outliers were removed and replaced with NaN values. To maintain the continuity of the time series, the NaN values were interpolated to fill in the missing data points with the interp function from the Python library NumPy. This function performs linear interpolation, estimating the values at the missing points based on the known data points surrounding them. The data was smoothed using a 56-day Hanning window convolution filter implemented with the multidimensional image processing package from the SciPy library in Python. The selection of a 56-day window was motivated by the aim to eliminate the influence of highly variable tidal currents beneath FIS, as observed in earlier studies Nicholls et al. (2009a); Hattermann et al. (2021). This filter effectively reduces short-term fluctuations in the data while preserving long-term variability. A convolution filter with a Hanning window acts as a moving average, where each data point is replaced with the average of its neighboring values within a specified window size (Rossant, 2018; Drentea, 2010). The Hanning window, constructed using the scipy.signal.windows.hann function from the SciPy signal processing package in Python ensures a smooth transition and helps avoid abrupt changes in the signal near the window boundaries. Applying the Hanning window reduces potential artifacts that can occur with other types of window functions (Drentea, 2010). Detailed information on the application of a Hanning Window can be found in App.7.1.

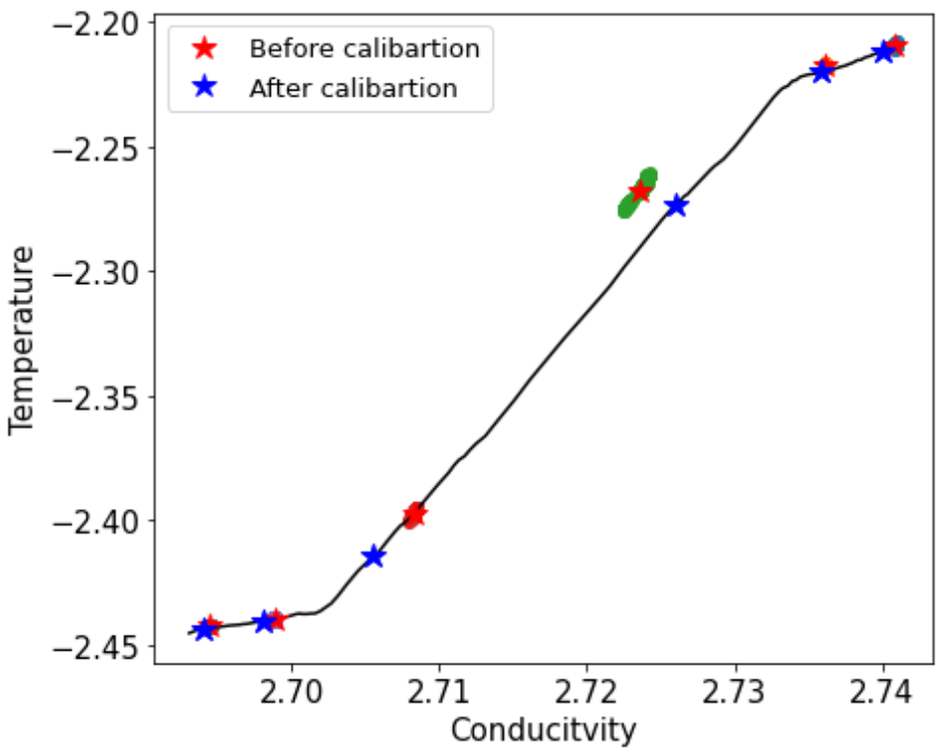

Figure 3.2: Temperature-Conductivity diagram displaying the calibration of the FSE2 mooring from the FSE2 CTD (black line). The red stars show the mean of the first 200 data points (approximately 30 minutes) for each instrument; the blue stars show the mean of the first 200 data points after calibration. The first 200 data points are also displayed for each instrument (blue, orange, green, and red dots).

The conductivity and temperature measurements obtained from the CTD and mooring were converted to practical salinity and potential temperature using the Python implementation of the Gibbs SeaWater (GSW) Oceanographic Toolbox based on the Thermodynamic Equation Of Seawater - 2010 (TEOS-10). The choice of practical salinity as a parameter was motivated by the possibility of comparing it with data from previous studies. The temperature was converted to potential temperature due to its ability to accurately represent the thermal characteristics of the water because it removes the effects of pressure and depth (McDougall et al., 2013).

For the velocity data, the magnetic declination was adjusted using the MATLAB toolbox for the International Geomagnetic Reference Field (IGRF) model, following the approach described by Hattermann et al. (2021). The velocity and backscatter data were smoothed with a 56-day Hanning window convolution filter. Additionally, when displayed as a time series and vertical velocity shear, the smoothed velocity data were averaged in 2 week-bins with the re-sample function from the Pandas library in Python.

3.1.2 Anomalies and 2D histograms

2D histograms were constructed to analyze the relationship between systematic velocity anomalies and systematic anomalies of potential temperature, source salinity, and back-scatter. First, the MicroCAT data and the ADCP data were interpolated on the time vector of the velocity data with the NumPy interp function. The anomalies of the different variables were calculated using a convolution filter from the multidimensional image processing package from the SciPy library in Python. A one-year Hanning window was subtracted from a 28-day Hanning window to filter out the background trend and the tidal cycles, resulting in a filtered signal that highlights localized variations or anomalies in the data. An example of the filtering of potential temperature is displayed in Fig.3.3a.

To construct the histograms, the Python library SciPy stat package function binned_statistic_2d was used (Lilly, Jonathan, 2023). The function constructs a 2D velocity diagram by dividing the space into bins and provides the count of velocity observations within each bin. All velocity observations less than ten are neglected. Further, the function calculates the mean of potential temperature anomalies, source salinity, and back-scatter within each bin for the corresponding velocity anomaly.

In order to investigate the magnitude and direction of variability within the velocity anomalies, variance ellipses were constructed for each histogram. The derivation of variance ellipses relies on the covariance matrix. A detailed ex-

planation of the method, including the necessary equations, can be found in App.7.2 and 7.3. This method involves computing the eigenvalues and eigenvectors of the covariance matrix. From these eigenvalues and eigenvectors, the semi-minor axis (a), semi-major axis (b), and orientation angle (θ) of the variance ellipse can be derived. The magnitude of the semi-major and semi-minor axes align with the variance, representing the extent of the data dispersion, where a larger axes coincide with a larger spread in the data. The orientation of the ellipse indicates the direction of maximum variability in the flow field. The variance ellipse, denoted by z, is represented by a collection of complex numbers that define its boundary:

$$z = \exp^{j\theta}(a\cos(\phi) - jb\sin(\phi)) \tag{3.1}$$

Where ϕ represents an array of angles ranging from 0 to 2π, a and b are the semi-major and semi-minor axis (Eq.7.8) and θ is the orientation (Eq.7.9). The velocity histogram and the associated variance ellipse are displayed in Fig. 3.3b. The histogram visually represents the distribution of velocity anomalies, while the variance ellipse overlays the histogram, illustrating the orientation, shape, and size of the data distribution.

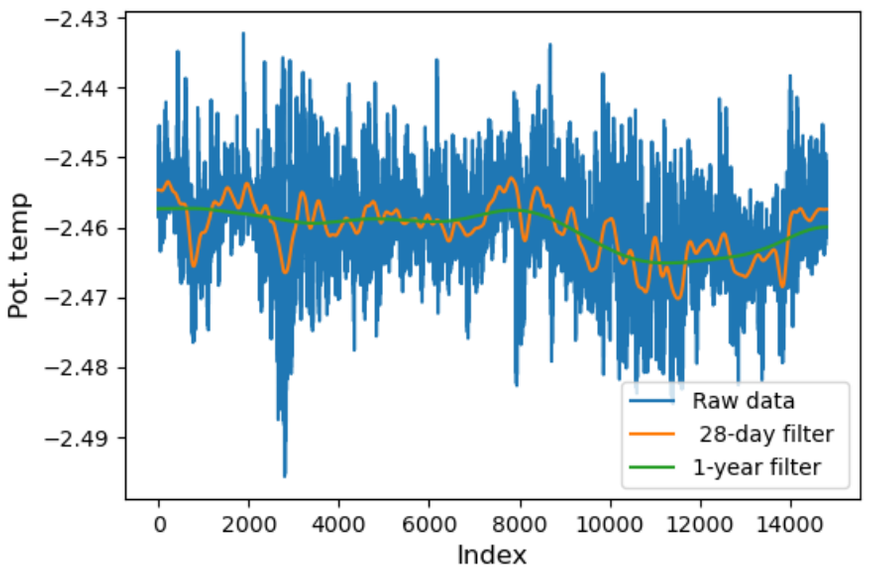

(a)

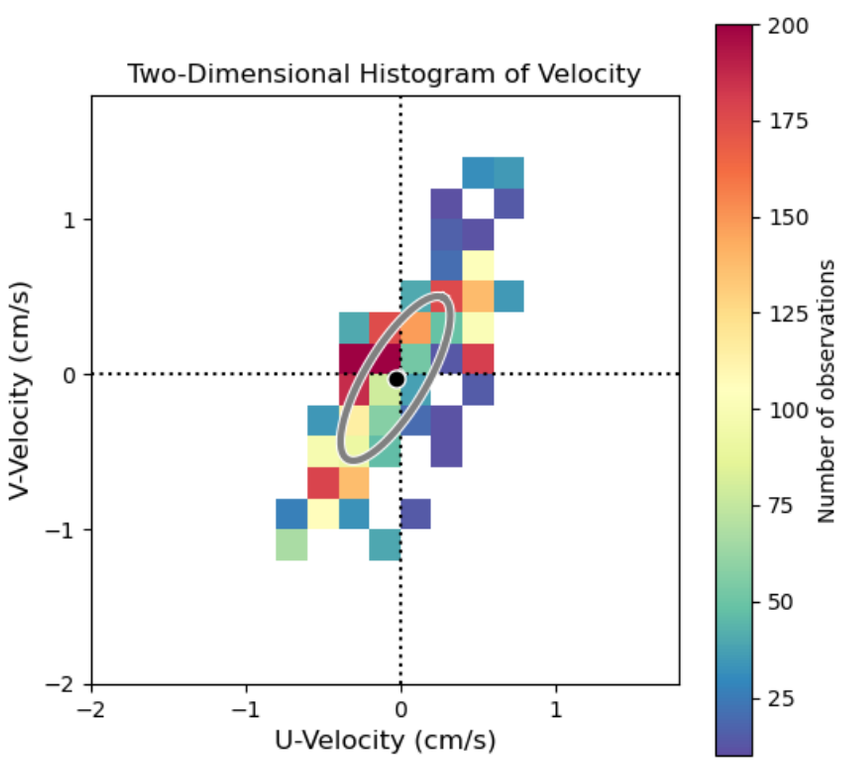

(b)

Figure 3.3: Panel (a) shows raw potential temperature (blue), the 28-day Hanning window filter of potential temperature (orange), and a one-year Hanning window of potential temperature (green). Panel (b) shows a 2D-histogram of velocity anomalies between 17.05.2019 - 20.07.2020. Observations of less than ten are removed and a variance ellipse is overlaid to display the data anomaly distribution.

3.1.3 Time Lags in backscatter

Two methods were used to compute the time lags in the backscatter signal between 750 m and 1150 m depths. First, the time lags were calculated by manually comparing peaks in the two-time series. The peaks were chosen based on the point where the graph stopped increasing rapidly. The time lags between the two signals were also calculated using cross-correlation with different Hanning windows to show how the filtering impacts the time lag results. The correlation coefficients measure the relationship between the two backscatter signals. The cross-correlation was calculated with the correlation coefficient function in the Python library NumPy. This function returns the Pearson Product-Moment Correlation (a measure of the strength of a linear association between two variables) in terms of a correlation coefficient matrix (R) of the variables and is expressed as: $R_{ij} = \frac{C_{ij}}{\sqrt{C_{ii}C_{jj}}}$, where C is the covariance matrix (Eq.7.5). The value of R ranges from -1 to 1. A value closer to +1 indicates a stronger linear relationship, while a value closer to -1 indicates a negative correlation between the variables (Mitchell, 2022). When computing the cross-correlation, the maximum time lag was chosen to be 30 days. Further, the mean value and the stander deviation of the time lags found by cross-correlation were calculated to measure the spread of the data distribution. The standard deviation was found with the NumPy std in the Python library, which calculates the square root of the variance. The stander deviation of the time lags represents how much the individual time lag differs from the average (see App.7.2)(Mitchell, 2022).

Assuming that increased sediments in the water cause the backscatter peaks, a falling velocity of the sediment can be found by dividing the time lag between the two backscatter signals by the vertical distance between the instruments at 750 m and 115 m. To calculate the falling velocities of the sediments, the time lag was used as the time it takes for the sediments to sink from 750 m to 1150 m, and the vertical distance between 750 m and 1150 m was used as the displacement. From the falling velocity the grain size can be determined from Fig.27 in Soulsby (1997)

3.2 Gade Line and Source Salinity

The Gade line makes it possible to determine the salinity of the source water due to the constraints of how seawater properties evolve in contact with the ice shelf base (Nicholls et al., 2009b). Assuming that the source water temperature equals the surface freezing point, the source salinity can be found where the Gade line intersects with the surface freezing point. From Eq.2.2 combined

with linear function theory, the rate of increase, a, is given by $\frac{L}{S_0 C_w}$ and the y-axis interaction for T(S = 0), b, can be expressed as $-\frac{L}{cw} + T_0$. The freezing point of water is dependent on salinity. Hence a linear surface freezing point function can be expressed as:

$$T_{freeze} = \frac{\Delta T_{freeze}}{\Delta S_{freeze}} * S + T_{0freeze}(S = 0) \tag{3.2}$$

Where ΔT_{freeze} and ΔS_{freeze} are chosen from values of freezing point temperatures of potential temperatures found with the TEOS-10 GSW package (-1.63°C and -1.89 °C) for particular salinities (30 psu and 34.6 psu) and $T_{0freeze}(S = 0)$ is ~ 0°C). By linear function theory, the intersection of Eqs. 2.2 and 3.2, hence the source salinity can be expressed as:

$$S_{source} = \frac{(T_{0freeze(s=0)} - (\frac{L}{c_w} + T_0))}{(\frac{L}{c_w S_0} - \frac{\Delta T_{freeze}}{\Delta S_{freeze}})} \tag{3.3}$$

L is the latent heat of fusion of ice ($3.35 * 10^5$ Jkg^{-1}), S_0 and T_0 is the salinity and temperature of the source water mass, c_w is the specific heat capacity of water (4000 J $kg^{-1o}C^{-1}$).

When determining the source salinity of ISW using potential temperature, it is essential to understand the impact of this method on temperature measurements. Fig.3.4 illustrates that when tracing ISW back to its source water when using potential temperature, a net temperature change of 0.004°C will be lost. This temperature loss is because the mixing process from the source water to ISW in the ice shelf cavity occurs at a higher pressure, which is not considered when calculating the potential temperature at zero pressure. A temperature loss of $0.004°C$ does not significantly affect the calculations of the source salinity of ISW. Thus, this factor is not considered further in this study.

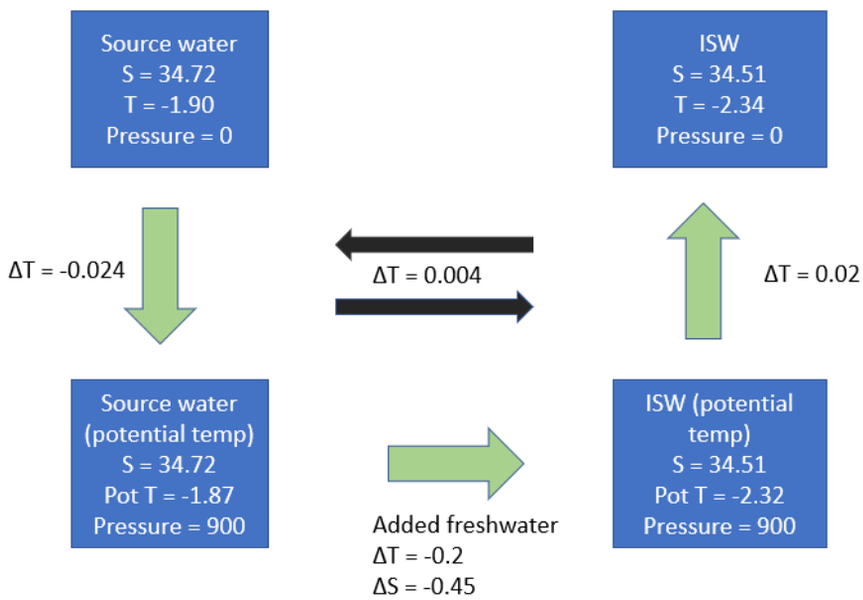

Figure 3.4: Illustration showing the transformation from source water to ISW when using potential temperature. The difference between source water measured in in-situ temperature and source water converted to potential temperature is -0.024 $^{\circ}C$. When source water is converted to ISW by mixing with freshwater (temperature and salt change form TS-diagram Fig. 4.2b) and then converted to in-situ temperature, the temperature difference is 0.02 $^{\circ}C$. The net temperature change when converting the ISW from 0 pressure back to its source at zero pressure, and the net temperature change of 0.004 $^{\circ}C$ will be lost.

3.3 Freshwater Content Estimations

To determine the fraction of subglacial runoff in relation to the total freshwater fraction within a CTD profile, an initial step involves calculating the fraction of freshwater within the observed profile and the fraction of freshwater caused by basal meltwater. The freshwater fraction, denoted as FW_f, could be found using a simple conservation assumption, where the total unit volume $1 = FW_f + W_0$ is the mixture of a source water fraction W_0 of salinity S_0 and a fraction of freshwater FW_f, and S denoting the salinity of the mixture. The fraction of freshwater is given as $FW_f = FW_b + FW_r$, where FW_b is the fraction of basal meltwater and FW_r is the fraction of subglacial runoff. Applying salt conservation principles makes it possible to determine the fraction of the freshwater, FW_f. Fig.3.5 illustrates three systems: box 1 contains only source water, box 2 includes freshwater from basal melt, and box 3 contains both basal melt and subglacial runoff. The principle of salt conservation states that the mass of salt in box 1 is the same as in boxes 2 and 3. This can be expressed as: $\rho_0 S_0 W_0 = \rho_0 S(FW_f + W_0)$. Following the Boussinesq approximation, a constant reference density rho_0 is used and drops out of the equation (Satoh, 2004). Thus, the fraction of the source water, W_0, can be expressed as: $W_0 = \frac{S}{S_0}$. This leads to the expression for the total freshwater fraction:

$$FW_f = (1 - \frac{S}{S_0}) \tag{3.4}$$

Where S_0 is the salinity of the source water, and S represents the salinity of the mixture of the source water and freshwater. To further separate the freshwater fraction into contributions from basal melting and subglacial runoff, the CTD profiles are analyzed in a temperature-salinity (TS) space. In Fig.3.6, Box 3 represents a hypothetical CTD profile that includes subglacial runoff and basal meltwater. The CTD profile is represented as a mixing line in the TS-diagram, illustrating the combined influence of subglacial runoff and basal melt on the temperature and salinity from the reference water mass (S_{ref}, T_{ref}), to the freshwater mixture (S_{mix}, T_{mix}). Eq.3.4 determines the total freshwater fraction within this theoretical CTD profile using $S_{ref} = S_0$ and $S_{mix} = \mathrm{S}$. The fraction of basal meltwater of the total freshwater can be derived from computing the Gade line (eq.2.2) from the reference water mass to a salinity S_b and temperature T_b. It can be assumed that $T_b = T_{mix}$. This is because the temperature change from T_{ref} to T_{mix} indicates the amount of heat that has been used to melt ice (considering that the effect of subglacial runoff on temperature is small because of the small relative amount of the freshwater that has been added $< 1\%$ Tab.4.1), which then is converted via the Gade-line relation into the amount of freshwater that has been added due to the melting. The corresponding salinity can be expressed as:

$$S_b = (T_{mix} + \frac{L}{c_w} - T_{ref})(\frac{L}{S_{ref} C_w})^{-1} \tag{3.5}$$

Where L and C_w are defined in Eq.3.3, the fraction of basal meltwater, FW_{btot}, in the modified freshwater mixture, can thus be calculated with Eq. 3.4 with $S = S_b$ and $S_0 = S_{ref}$. Thus, the fraction of basal melt in the total freshwater content is expressed as

$$FW_b = \frac{FW_{btot}}{FW_f} = \frac{S_{ref} - S_b}{S_{ref} - S_{mix}} \tag{3.6}$$

By $FW_f = FW_b + FW_r$, and assuming that $FW_f = 1$, the subglacial runoff fraction of the total freshwater content can be expressed as:

$$FW_r = 1 - FW_b \tag{3.7}$$

Calculating the subglacial runoff fraction within the upper layers of the CTD profiles involved selecting S_{ref} and T_{ref} as the salinity and temperature measured in the bottom layer. Additionally, S_{mix} and T_{mix} were chosen as the salinity measured at the ice shelf base. The subglacial freshwater fraction has also been calculated by tracing the water mass back to its original source via the Gade line, with defining the source water mass by Eq.3.3 for salinity and Eq.3.2 (~ -1.9 assuming the source water is HSSW) for temperature.

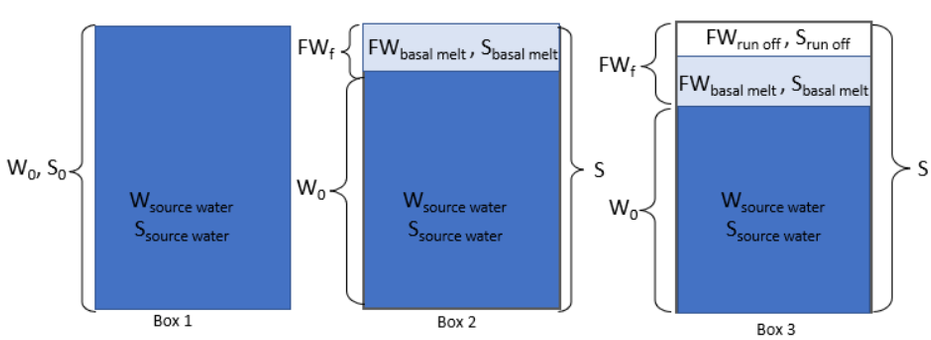

Figure 3.5: The system used to describe the derivation of freshwater content in the upper layer. Box 1 contains only source water, box 2 contains source water and freshwater from basal melt, while box 3 contains source water, basal melt, and subglacial runoff. FW_f marks the volume of the freshwater layer, W_0 and S_0 mark the volume and salinity of the layer containing source water, and S marks the salinity in the upper layer when freshwater is added.

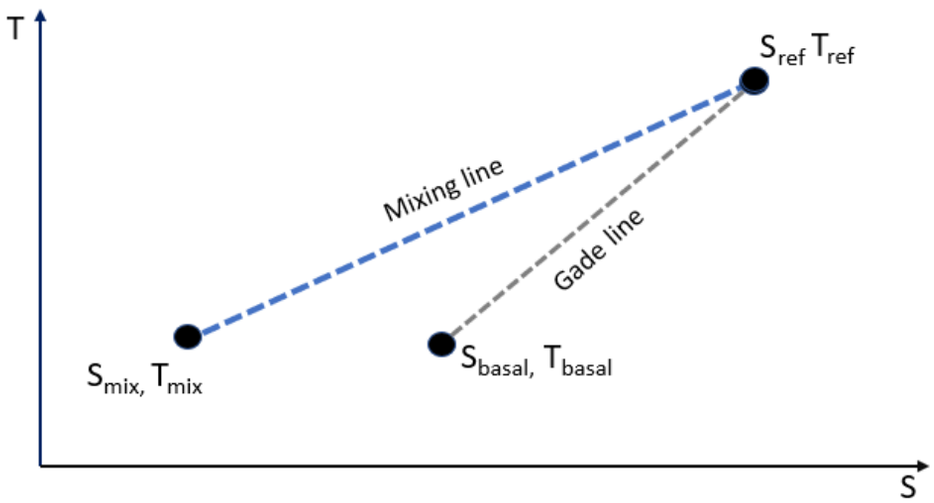

Figure 3.6: TS-diagram showing a theoretical CTD profile containing subglacial runoff and basal meltwater (box 3 in Fig. 3.5). S_{ref} and T_{ref} are the salinity and temperature of the source water mass, S_{basal} and T_{basal} are the salinity and temperature of the source water mass when following the Gade line (Eq.2.2), and S_{mix} and T_{mix} is the salinity and temperature of the freshwater mixture.

3.4 Freshwater Flux

Using the CTD data and the mooring data at FSE2, an approximation of the freshwater flux from SFG entering the sub-ice shelf cavity can be found. This is done by assuming that both the basal melt rate and the current velocity within the ice shelf cavity are constant, that a basal meltwater channel extends from the grounding line to the position of FSE2, and that the width of the channel is half of the distance between FSE2 and FSE1. These assumptions give rise to estimations of the volume of freshwater due to basal melt within the meltwater channel, which can be determined by:

$$V_{bmelt} = \int_A \int_{t_0}^{t_1} m(t, A) * \frac{\rho_w}{\rho_i} \, dt dA = m * t * A * \frac{\rho_w}{\rho_i} \tag{3.8}$$

Where m is the average basal melt rate of 0.25 ma^{-1} of the meltwater channel at FIS ice shelf, extracted from Zeising et al. (2022); ρ_w and ρ_i are the density of freshwater (997 kg m^{-3}) and sea ice (917 Kgm^{-3}); A is the total surface (dA = y dx) of the meltwater channel, where length (182 km) and width (15 km) of the meltwater channel is measured in Qgis (Fig. 3.8); t is the time it takes for a water mass to be transported from the grounding line of SFG to FSE2. The time is determined from mean velocity measurements at FSE2 and the length of the

meltwater channel (t = 50 days). A 56-day Hanning-window convolution filter of the velocity and the mean of the filtered velocity at all depths are displayed in Fig. 3.7. The 750 m and 840 m instruments are situated near the ice shelf base, making them prone to turbulence, which can reduce the mean velocity. The travel time from the grounding line to the FSE2 station is estimated to be 318 days and 287 days at depths of 750 m and 840 m, respectively, which is considered excessive. Therefore, velocities at greater depths are more accurate for representing the approximation of the overall flow. The mean of the filtered velocity at 1008 m is further used in the approximation, resulting in a travel time of 50 days.

The flux of basal meltwater, Fl_{bmelt}, can be obtained by dividing by the time (t) on the volume of basal meltwater (Eq. 3.8). The division by time excludes the time variable, rendering the choice of mean velocity at a certain depth irrelevant to the flux estimation. The basal meltwater flux is thus expressed as:

$$Fl_{bmelt} = m * A * \frac{\rho_w}{\rho_i} \tag{3.9}$$

The total flux of freshwater can be determined by combining equations 3.9 and 3.6. By calculating the basal meltwater flux as a percentage of the total freshwater flux, it is possible to ascertain the overall flux of freshwater. Hence, the total freshwater flux can be expressed as:

$$Fl_{tot} = Fl_{bmelt} * \frac{S_{ref} - S_{mix}}{S_{ref} - S_b} \tag{3.10}$$

When the total volume of freshwater and basal meltwater is known, it becomes possible to determine the flux of subglacial runoff $Fl_{srunoff}$ passing FSE2 via the meltwater channel

$$Fl_{srunoff} = Fl_{tot} - Fl_{bmelt} \tag{3.11}$$

To demonstrate the variability in the calculations, three source water masses of potential temperature and salinity were chosen in Eqs. 3.10 and 3.11 when applied to the mooring data. The first source water mass was selected at 1150 m depth, the second source water mass as the mean values of 1550 m and 1080 m, and the third source water mass as the mean values of 1550 m, 1080 m, and 1006 m. Measurements at 750 m depth were used as the final salinity, S. The data were interpolated on the same time vector before a cross-correlation between 750 m and the source water masses was done. The cross-correlation analysis indicated the highest correlation coefficient at the beginning of the time series, indicating that no time shift was required between the two-time series.

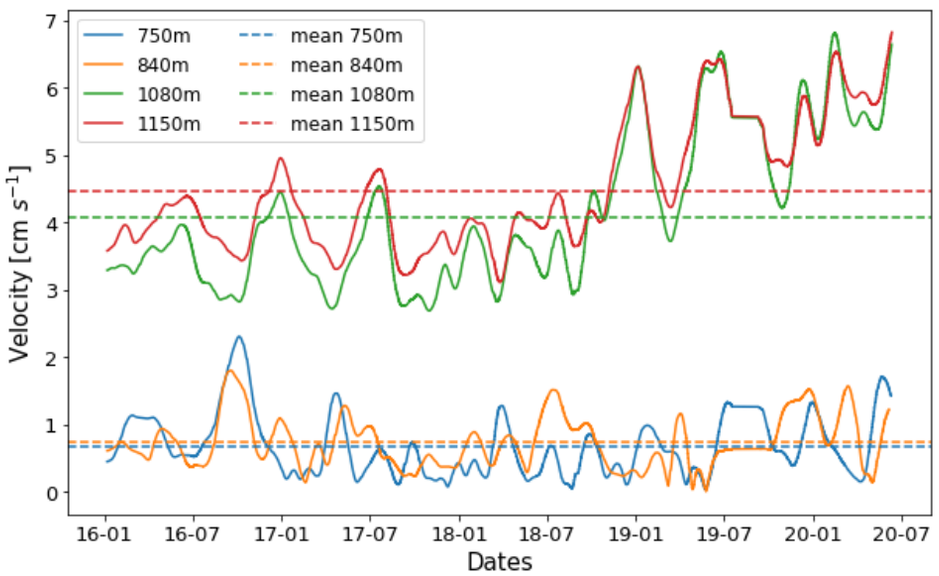

Figure 3.7: Low pass filtered velocity data from the FSE2 mooring. Filtered with a 52-day Hanning-window convolution filter. The mean velocity of each filtered time series is displayed as the dashed line. X-axis showing dates yy-mm.

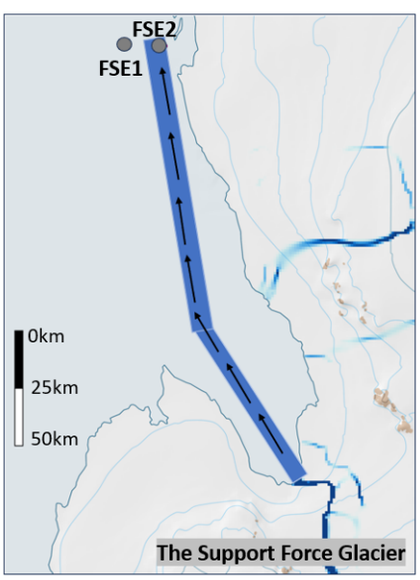

Figure 3.8: Map of the meltwater channel (blue area) from the SFG to FSE2, with glacier runoff flowing from the grounding line to FSE2 within the channel. The length (182322 m) and width (15796 m) of the channel are measured in Quantartica (Norsk Polarinstitutt, 2023).

4

Results

4.1 Freshwater Content

The CTD profiles taken at FSW1, FSW2, FSE1, and FSE2 all show a two-layer stratification, characterized by a deep layer containing a less modified ISW (salinity of 34.61) and a fresher upper layer containing strongly modified ISW (Fig. 4.1). The FSE2 profile stands out from the others due to a less saline and warmer upper layer. The Gade lines, computed using Eqs.2.2 and 2.3, show that the potential temperature and salinity profiles of FSW2 and FSE1 are close to the Gade lines, while in FSW1 and FSE2, the potential temperature and salinity deviate from the Gade lines in the upper layer. Notably, FSW1 and FSE2 profiles were located in areas of a thinner ice shelf, with an ice base pressure of 751 m at FSW1 and 735 m at FSE2. Despite both FSW1 and FSE2 deviating from the Gade lines, the profile of FSE2 demonstrates the most distinctive features.

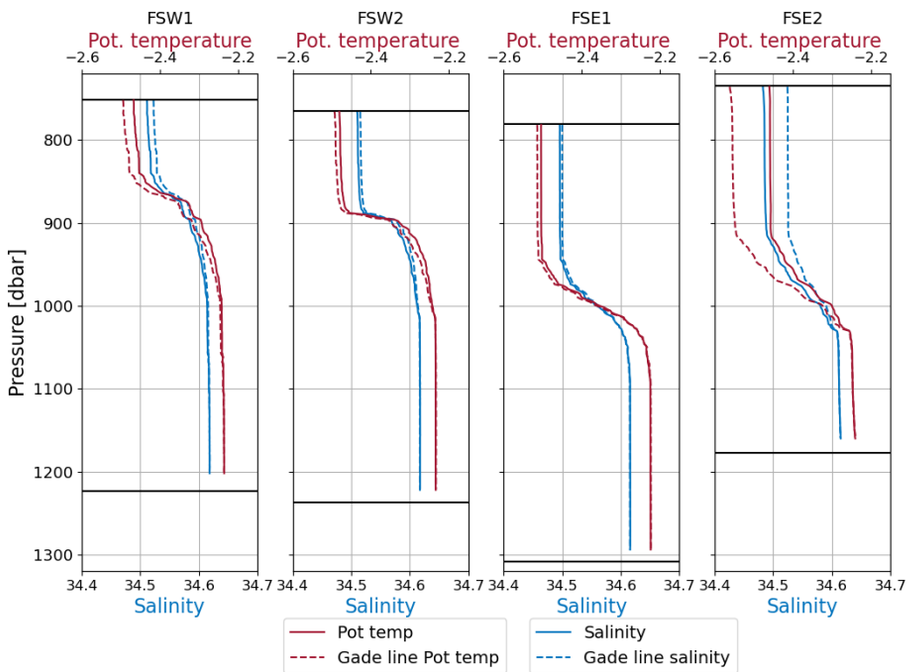

Figure 4.1: Vertical profiles of potential temperature (red) and practical salinity (blue). From left to right: FSW1, FSW2, FSE1, FSE2. The dashed red and blue lines represent the theoretical Gade lines for potential temperature and salinity, respectively, and are calculated by Eq. 2.3 and Eq. 2.2. The horizontal upper lines mark the ice base pressure, and the horizontal bottom lines mark the depth of the seabed.

To further investigate the freshwater content in the FSE2 system, a TS-diagram comparing the FSE2 and FSE1 CTD profiles and their corresponding Gade lines (estimated with Eq.2.2) is presented in Fig.4.2. Consistent with the vertical CTD profiles, FSE2 is found to exhibit a fresher profile compared to FSE1. Additionally, FSE2 exhibits a clear fresher deviation from its Gade line, indicating a substantial influence of freshwater in this region. With the use of Eqs.3.4, 3.6 and 3.7 and considering the salinity properties of the deep layer as the source water and the salinity at the ice shelf base as the freshwater mixture, the fractions of freshwater within the upper layer was obtained. The percentage of total freshwater content and its breakdown into contributions from basal melt and subglacial runoff at FSE1 and FSE2 are summarized in Tab. 4.1. The analysis indicated that at FSE1, the freshwater fraction was 0.34%, with 96.49% attributed to basal melt and 3.51% contributed by subglacial runoff. Similarly, at FSE2, the freshwater fraction was 0.38%, with 68.39% attributed to basal melt and 31.50% contributed by subglacial runoff. Fig. 4.2b provides insights into the source water of the water masses in FSE1 and FSE2 via the Gade line. The intersection of the Gade line and the freezing point temperature corresponds to

a source salinity of 34.74 for FSE1 and 34.75 for FSE2, falling within the range of HSSW salinity. Calculating the freshwater content with the source salinity as a reference reveals a total freshwater content of 0.73% in FSE1 and 0.78% in FSE2. In FSE1, basal melt contributes to 98.32% of the total freshwater content, while subglacial runoff accounts for 1.67%. In FSE2, basal melt accounts for 84.43% and subglacial runoff accounts for 15.56% of the total freshwater content.

Table 4.1: Total percentage of freshwater, and how much of this stems from basal melt and subglacial runoff at FSE1 and FSE2. The local system refers to percentages calculated using the deep layer salinity as source water mass.

	FSE1	**FSE2**
Total freshwater (local system)	0.34%	0.38 %
Basal Melt (local system)	96.49%	68.39%
Subglacial Runoff (local system)	3.50%	31.51%
Total freshwater (source water as reference)	0.73%	0.78%
Basal Melt (source water as reference)	98.32%	84.43%
Subglacial Runoff (source water as reference)	1.67 %	15.56%

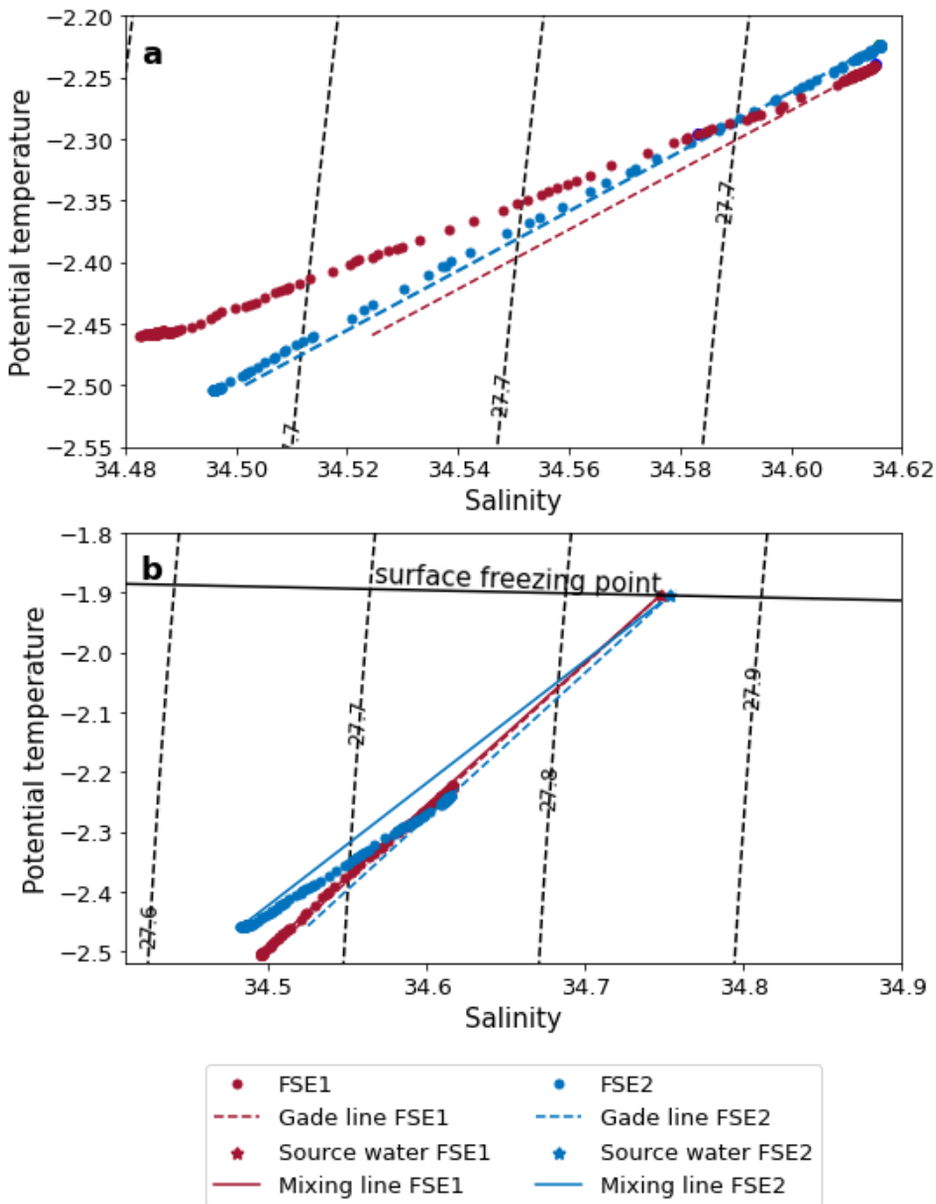

Figure 4.2: Panel (a) displays a TS-diagram of the CTD profiles of the local systems of FSE1 (red) and FSE2 (blue). A theoretical Gade line for each profile is calculated with Eq. 2.3 and used to determine the fraction of freshwater in the profiles. Panel (b) displays a TS-diagram of the CTD profiles of the water masses in FSE1 and FSE2, which are traced back to the source water. The intersection of the Gade line and the surface freezing point line gives the source salinity of 34.74 for FSE1 and 34.75 for FSE2. A mixing line (blue and red line) from the source water to the freshwater mixture in the upper layer is used to determine the fraction of freshwater with the source salinity as the source water mass.

4.2 General Conditions at FSE2

Fig.4.3 provides an overview of the temporal evolution of potential temperature, salinity, source salinity, velocity, and backscatter at FSE2 from January 2016 to December 2022. A two-layer stratification can be observed in potential temperature, salinity, and source salinity. Consistent characteristics of denser water were observed at 1150 m, 1080 m, and 1006 m depths. The water exhibited warmer temperatures, higher salinity, and higher source salinity values than the upper layer, indicating the presence of less modified ISW. The salinity and source salinity at 1080 m and 1006 m are higher than at 1150 m. This difference results from instrument drift or other measurement artifacts. The measurements at 930 m, 840 m, and 750 m indicate colder water with lower salinity and source salinity values than the bottom layer, indicating the presence of a strongly modified ISW. The potential temperature, salinity, and source salinity at 1150 m and 1080 m have an increasing trend from January 2017 to June 2020 before stabilizing. The middle two instruments, 1006 m and 930 m, show more variability over time. Furthermore, an increasing trend in source salinity is observed at 840 m and 750 m from July 2018 to June 2019, accompanied by fluctuations that can be traced back to events of subglacial runoff, which are further analyzed in the next section.

The mean current velocity measured at 1150 m and 1080 m is consistent in a northeast direction and becomes stronger from December 2018 until July 2020. The mean current velocity at 750 m and 840 m is more varying and flows northward from January 2016 until May 2018 and switches to a southward mean current from May 2018 until July 2020. There is a varying, but the same signals can be seen for all depths. The strongest signal is at 1150 m, and the weakest is at 750 m.

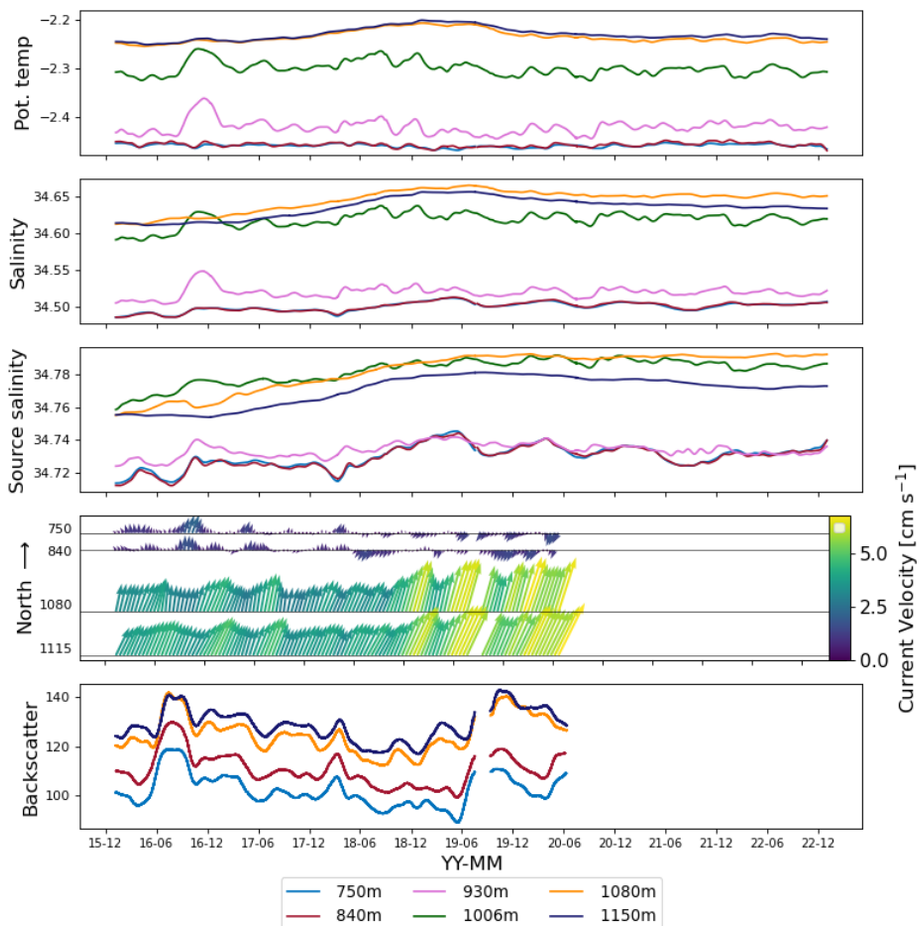

Figure 4.3: Time series from 06.01.2016 - 31.12.2022 (20.07.2020) (dd.mm.yyyy) of potential temperature [θ], salinity [psu], source salinity [psu], velocity [cm s^{-1}], and backscatter [dB] at FSE2 from 750 m, 840 m, 930 m, 1006 m, 1080 m, and 1115 m depths. The y-axis on the velocity panels displays instrument depth in meters. Dates on the x-axis show yy-mm

4.3 Subglacial runoff events at FSE2

Fig.4.4 illustrates the relationship between pulses of subglacial runoff events and time series of potential temperature, source salinity, velocity, and backscatter, at 750 m and 840 m depths. In this thesis, the subglacial runoff event refers specifically to events detected in the source salinity, where the source salinity first rapidly decreases (phase 1), followed by a rapid increase in source salinity (phase 2).

Six subglacial runoff events were detected from January 2016 until Decem-

ber 2022. The minimum in source salinity during the subglacial runoff event marks the end of phase 1. Phase 1 is characterized by a lower source salinity, associated with a peak in potential temperature and backscatter. Phase 2 is characterized by a sharp increase in source salinity following phase 1. This increase in source salinity coincides with a decrease in potential temperature and backscatter. The maximum source salinity in the subglacial event marks the end of phase 2. Tab. 4.2 presents the start- and end time of each subglacial runoff event, determined by when the rapid decrease start in source salinity and from when the rapid increase of source salinity within the event stops. The date of minimum source salinity marking the end of phase 1 and maximum source salinity marking phase end of phase 2 is also presented in the table. From January 2016 to May 2018, the mean velocity of the current is consistent

Table 4.2: Number of subglacial runoff events, starting and ending date of each event, date of minimum source salinity (phase 1), and maximum source salinity (phase 2) within each event.

Event	Starting Date	Ending Date	Minimum Source Salinity (Phase 1)	Maximum Source Salinity (Phase 2)
1	Unknown	07.04.2016	06.01.2016	07.04.2016
2	07.04.2016	19.10.2016	25.07.2016	19.10.2016
3	21.12.2017	24.04.2018	12.03.2018	26.04.2018
4	11.05.2019	28.03.2020	05.09.2019	28.03.2020
5	28.03.2020	04.02.2021	08.08.2020	02.01.2021
6	04.02.2021	09.02.2022	27.08.2021	09.02.2022

in a northward direction. Local variation is observed, which coincides with the subglacial runoff event. An increase in current velocity was observed for both depths during phase 2, when the source salinity rapidly increased, accompanied by a change in the current direction towards the northeast at 750 m. At the same time, a stronger northward current was observed at 840 m. In May 2018, as the source salinity started to have an increasing trend, the mean current changed direction towards the south. The southward propagation of the mean current stayed consistent until July 2020 (the end of the velocity time series). During a subglacial runoff event in this period, the southward mean current weakened during phase 2.

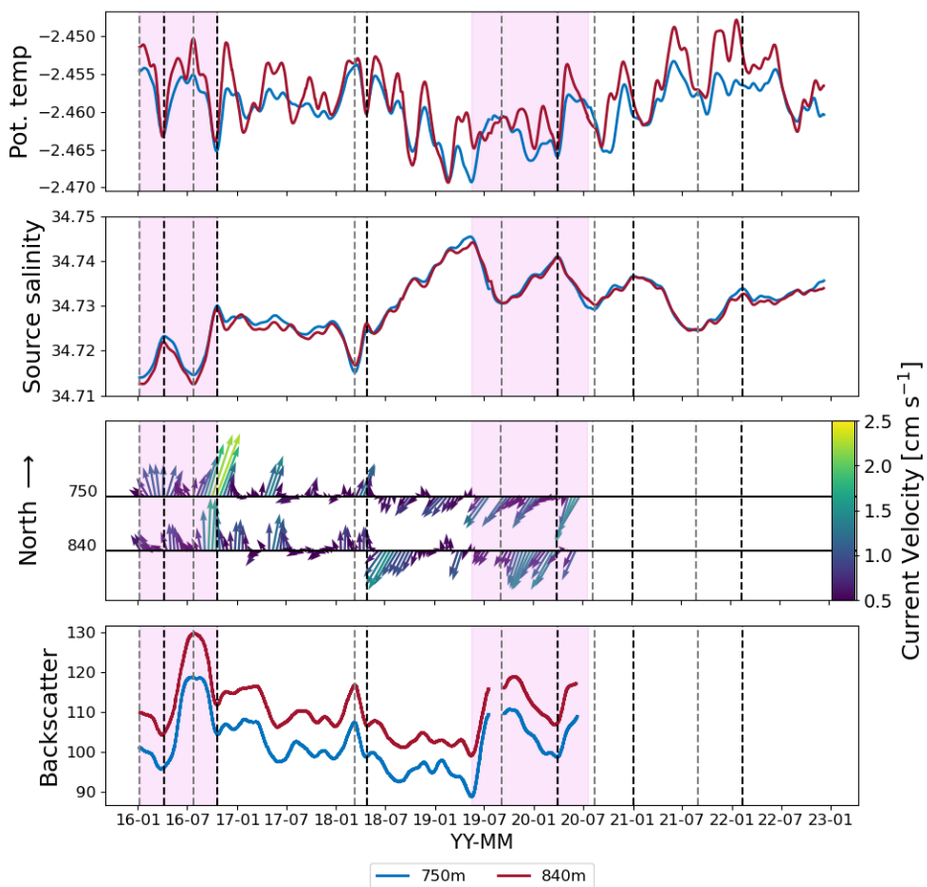

Figure 4.4: Time series of potential temperature [θ], source salinity [psu], velocity [cm s^{-1}], and backscatter [dB] at FSE2 from 750 m and 840 m depths. The y-axis on the velocity panels displays instrument depth in meters. Grey lines mark minimum values of source salinity, and black lines mark maximum values of source salinity followed by a minimum value. The pink shade marks the two intervals: 06.01.2016 - 18.10.2016 and 17.05.2020 - 20.07.2020 (dd.mm.yyyy). Dates on the x-axis show yy-mm.

Further investigation of how the subglacial runoff event affects the mean current is done in two different time intervals. The first interval is characterized by a northward propagation of the mean current, and the second interval shows southward propagation in the upper layer. The first period spans from the 6th of January 2016 to the 18th of October 2016, while the second interval spans from the 17th of May 2020 to the 20th of July 2020 (highlighted in pink in Fig. 4.4).

For the two phases of the subglacial runoff event during both intervals, a 2-week binned average of 2-month filtered velocity data is shown for all depths

in Fig. 4.5. The representation of each phase is chosen close to the minimum values of source salinity for phase 1 and close to the maximum value of source salinity for phase 2 (Tab. 4.2). Fig. 4.5a represents phase 1 in a subglacial runoff event in the first interval. The velocity is a binned average from the 29th of May to the 12th of June, 2016. The analysis shows a vertical velocity shear that rotates counterclockwise with height, decreasing velocities from the bottom toward the ice shelf base. Phase 2 of the subglacial runoff event in interval 1 is shown in Fig. 4.5c and is a binned average of the velocity from the 2nd to the 16th of October 2016. A vertical velocity shear rotating counterclockwise is observed between 1115 m, 1080 m, and 840 m, where the velocity decreased from the bottom toward the ice shelf base. However, the mean current at 750 m deviates from this vertical velocity shear by increased velocity and a changed direction towards the northeast. Phase 1 of the subglacial runoff event in the second interval is seen in Fig. 4.5b, showing a binned average from the 7th to the 21st of July 2019. A vertical velocity shear rotating counterclockwise with height is also observed. The velocity shear initially decreases with height but then reverses direction and starts to increase again. Phase 2 within interval 2 is illustrated in Fig. 4.5d, displaying a binned average from the 27th of October to the 10th of November 2019. The mean current direction at 750 m diverges from the vertical velocity shear observed during phase 1 of this interval. Additionally, this deviation is accompanied by a decrease in velocity at 750 m.

The histogram in Fig. 4.6 presents the relationship between velocity anomalies and anomalies of potential temperature, source salinity, and backscatter during the two intervals at 750 m (marked in pink Fig. 4.4). In the first interval, strong northeast velocity anomalies are linked to negative potential temperatures, positive source salinity, and negative backscatter anomalies. These anomalies are indicative of an ISW plume. Slower northwest and southwest velocity anomalies are associated with positive potential temperatures, negative source salinity, and positive backscatter anomalies, indicating subglacial runoff. The variance ellipse displays the strongest anomalies in the northeast direction. The anomalies in interval 2 show the same features as in interval 1. The variance ellipse is slightly towards the southwest.

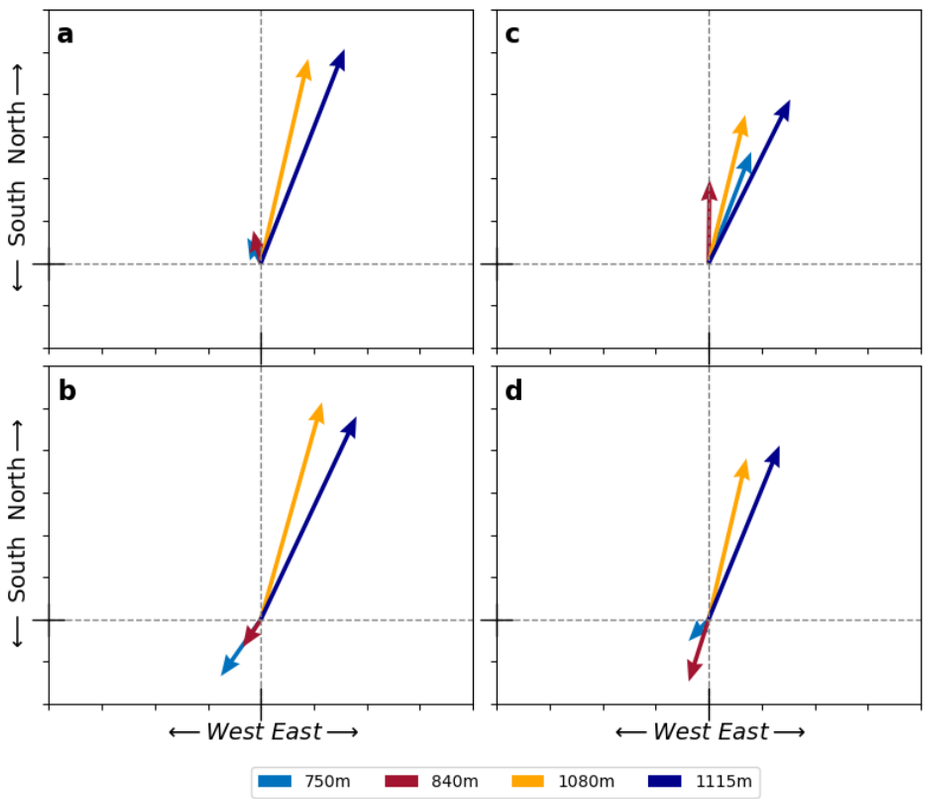

Figure 4.5: Vertical velocity shear between 750 m, 840 m, 1080 m, and 1115 m depth from a 2-week binned average of a 2-month lowpass filtered velocity data. (a) and (b) show an instance of low source salinity (marked with a grey dashed line in Fig.4.4), where (a) represents the first pulse observed in interval 1 (29.05.2016-12.06.2016) and (b) represents the observed pulse on interval 2 (07.07.2019-21.07.2019). (c) and (d) shows an instance of increased source salinity, where (c) represents the second peak in interval 1 (02.08.2016-16.08.2016) and (d) represents the first peak in interval 2 (07.07.2019-21.07.2019).

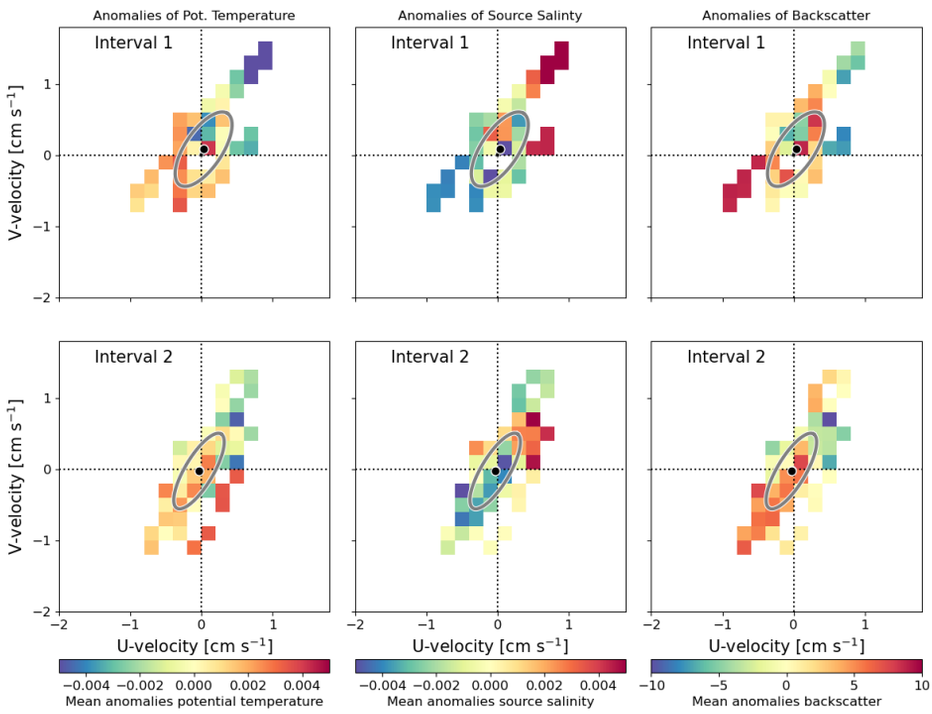

Figure 4.6: 2D histograms of velocity anomalies where each velocity bin contains the mean of potential temperature (left panel), source salinity (middle panel), and backscatter (right panel) anomalies. The upper row displays the anomalies from interval 1, and the lower row show anomalies from interval 2 (marked with pink in 4.4). All histograms have a variance ellipse showing the velocity anomalies' distribution.

4.4 Time Lag of backscatter

Fig. 4.7 presents the time lag observed between 750 m and 1150 m of the backscatter signal. The delayed back-scatter signal with depth indicates that the signal originates from a material falling vertically from the ice shelf base to the bottom. The time lag determined by identifying the peaks is displayed in the left panel. In contrast, the right panel shows the time lag calculated using cross-correlation with three different filtering windows. In the left panel, a time lag between the two depths is found to be 13 days and 22 hours (interval 1 in Fig. 4.4), and the second peak (interval 2 in Fig. 4.4) show a delay of 15 days. Assuming that sediments cause the backscatter peaks, the falling velocity of the sediment in peak one is 0.032 cm s^{-1} and 0.030 cm s^{-1} for peak 2. The falling velocity of 0.030 cm s^{-1} corresponds to a grain size of 0.02 mm (Soulsby,

1997)

Using cross-correlation (right panel), the 1-month, 2-month, and 3-month filters show time lags of 15 days, 14.4 days, and 13.5 days. The average time lag of all three filters is 14.3 days with a standard deviation of 0.61, which gives a falling velocity of 0.032 cm s^{-1}

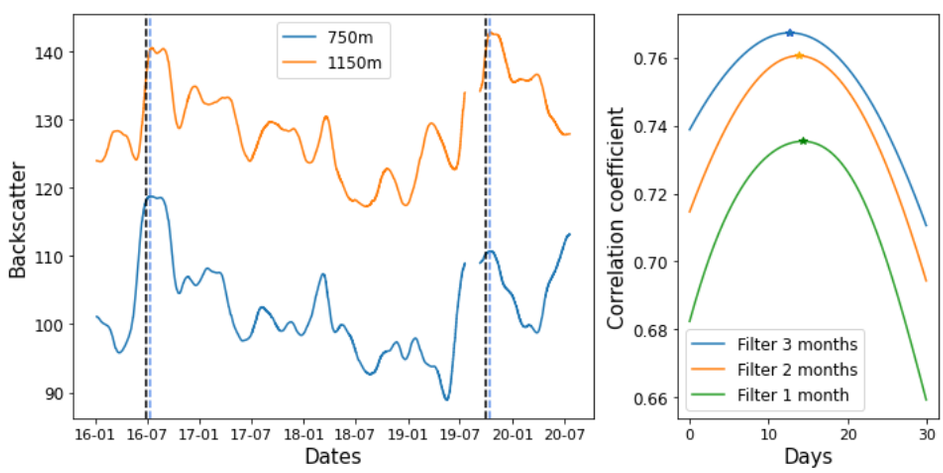

Figure 4.7: The left panel shows time series of backscatter [dB] at 750 m and 1150 m depth at FSE2. The black line marks the peak at 750 m, while the blue line marks the peak at 1150 m. The right panel shows the time lag calculated with cross-correlation with filtering windows of 3, 2, and 1 month. Maximum correlation is chosen to be 30 days.

4.5 Freshwater Flux

By Eq.3.9, the basal meltwater flux within the meltwater channel was calculated to be 12.4 m^3 s^{-1}. The subglacial runoff flux determined from the freshwater content (Tab.4.1) is found to be 5.72 m^3 s^{-1} and a total freshwater flux of 18.13 m^3 s^{-1}.

Fig. 4.8 displays a time series of freshwater content (calculated by Eq. 3.4), subglacial runoff percentage (calculated by Eq.3.7), and subglacial runoff flux at FSE2 (calculated by Eq.3.11), calculated using three different reference salinities and potential temperatures (lower instruments in Fig. 4.3). The time series reveals six distinct events characterized by increased freshwater content, subglacial runoff percentage, and enhanced freshwater flux, which align with the identified subglacial runoff events in Fig.4.4. The peaks of freshwater content and subglacial runoff coincide with the minimums source salinity during the subglacial runoff event, as indicated in Table 4.2. The choice of source water

mass influences the magnitude of the percentage of glacier runoff and subglacial runoff flux. Specifically, the source water mass obtained from a depth of 1115 m yields the lowest values for these variables. On the other hand, taking the mean values of 1150 m, 1080 m, and 1006 m as the source water mass results in the highest values for the percentage of glacier runoff and subglacial runoff flux. Additionally, the source water mass derived from the mean values of 1150 m and 1080 m exhibits the highest freshwater content.

The analysis of freshwater content reveals fluctuations ranging between 0.32% and 0.45%, encompassing all reference water masses. Additionally, an overall increasing trend is observed from January 2017 to August 2018. Similarly, both the subglacial runoff percentage and subglacial runoff flux exhibit similar patterns. An increasing trend is observed from January 2017 to August 2018 and a decreasing trend from April 2018 to April 2019. The subglacial runoff percentage varies between 20% and 42%, while the peaks of the subglacial runoff flux range between 3 and 9 $m^3\ s^{-1}$.

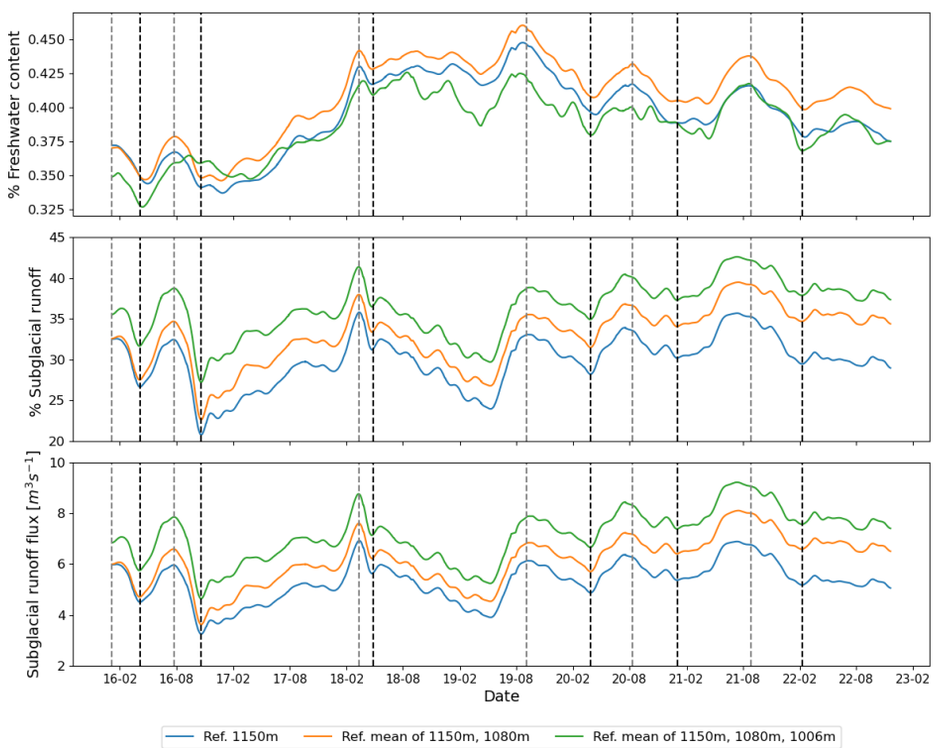

Figure 4.8: Time series of percentage of freshwater content (upper panel), percentage of subglacial runoff (middle panel), and subglacial runoff flux (lower panel). Grey dashed lines indicate minimum source salinity within a subglacial runoff event, and black dashed lines indicate maximum source salinity during a subglacial runoff event marked with black lines (as marked in Fig.4.4, Tab.4.2).

5

Discussion

5.1 Impacts of Subglacial Runoff on Water Transformation at the Eastern and Western Flanks beneath Filchner Ice Shelf

CTD analysis confirms that freshwater from subglacial runoff spreads on the western and eastern flanks beneath FIS (Fig.4.1). The subglacial runoff detected at FSE2 is proposed to originate from the grounding line of SFG. The subglacial runoff, having a lower density than the surrounding seawater, experiences buoyancy forces that cause it to ascend along the sloping ice shelf base, forming a buoyant plume. The buoyant freshwater plume preferentially flows towards the thinnest areas of the ice shelf. Since the ice shelf gradually thins towards its edges, the buoyant subglacial runoff naturally moves upward, primarily towards the east. The Coriolis effect will further constrain the buoyant plume's pathways if the plume's volume and velocity grow large enough (Holland and Feltham, 2006). Consequently, the plume exhibits geostrophic characteristics as it ascends along the ice shelf base, aligning with geostrophic flow patterns. In Hattermann et al. (2021) (updated based on Nicholls et al. (2009a)), the analysis of water column thickness contours and gradients reveals the presence of geostrophic flow directions towards the northeast. This flow pattern guides the plume to follow the topography on the eastern side of the Filchner Trough toward the north. Subsequent sections will provide a more comprehensive examination of the plume formation and its implications on the circulation observed at FSE2. The subglacial runoff observed at FSW1 is

hypothesized to originate from a different source, suggesting a different pathway for this subglacial runoff component which will not be further discussed.

The assessment of the subglacial runoff fraction at FSE2 involves considering both the local system and the reference water mass (Tab.4.1). In one case, it is examined how ISW that is present in the lower layer at FSE2 is further modified by basal melting and subglacial runoff in the local system, in the other case, the properties of the upper layer at FSE2 are compared to the HSSW source water outside of the ice shelf cavity. When examining the local system, the temperature and salinity properties in the bottom layer are assumed to be the source water mass of the transformed water mass observed in the upper layer. The source water mass is assumed to originate from areas further upstream within the cavity, consisting of HSSW that has experienced modifications due to basal melting along the Gade line, forming a less modified ISW. By analyzing the percentage of subglacial runoff from a water mass originating from areas further upstream in the cavity, the estimations reflect the extent of transformation along its pathway. Considering that the water mass in the lower layer at FSE2 is representative of the source water mass at the grounding line, it is demonstrated that the water mass in the upper layer at FSE2 has been modified by an admixture of 0.38% of freshwater that originates from basal melt and subglacial runoff. The deviation of the water mass transformation from the Gade line further indicates that subglacial runoff accounts for 31.50% of the freshwater content that has been added during this transformation. In contrast, when the water mass is traced back to its source, the analysis accounts for any basal melt mixed with the HSSW throughout its entire journey, starting from its entry into the ice shelf cavity at RIF and ending at the upper layer at FSE2. This approach indicates that the water mass has been transformed by an admixture of 0.78% of freshwater due to the combined effects of subglacial runoff and basal melt during this pathway. This approach indicated that 15.6 % of the freshwater could be attributed to subglacial runoff. This estimate is close to the previous measurements conducted in January 2016 by Huhn et al. (2018), who estimated subglacial runoff to be 13% of the freshwater content at FSE2 from noble gas samples. Hence, supporting the validity of the results in this study.

5.2 Subglacial Runoff Dynamics and Flux Variability

The subglacial runoff flux estimates obtained in this study show a range between 3 and 9 $m^3 s^{-1}$, which represents a higher discharge compared to the model results reported by Dow et al. (2022). The model findings by Dow et al.

(2022) indicated a discharge of 0.51 and 0.45 m^3s^{-1} from two small subglacial channels at SFG. Although the numerical values differ, the order of magnitude remains consistent. Both studies emphasize the persistent nature of the subglacial channels draining water beneath the ice streams and glacier catchments. As highlighted in Dow et al. (2022), these channels exhibit consistent size and distribution, remaining resistant to changes in sensitivity tests. Similarly, this study indicates a constant presence of subglacial runoff at FSE2. This is supported by the stratification in source salinity, with fresher source salinity in the upper instruments compared to the lower instruments at FSE2 (Fig.4.3), suggesting distinct origins or different mixing processes occurring within the ice shelf cavity system. Additionally, the approximation of the subglacial runoff flux at FSE2 further proposes the presence of a consistent subglacial runoff flux. The formation of subglacial basal melt, driven by geothermal heating at the glacier ice base and frictional heating from ice sliding over the bedrock, is a plausible explanation for this consistent discharge.

The time series analysis of the freshwater flux model reveals the occurrence of six distinct subglacial runoff events in a period of seven years. The events typically last for 264 ± 90.74 days, and the average time between individual events is 235±193 days. The extended duration and high standard deviation of the subglacial runoff event can be attributed to the challenge of precisely defining its start and end time. The occurrence of pulses does not follow a distinct seasonality, and the temporal variability in event occurrence ranges from mutilmonth to interannual timescales. Instead, it is expected that the timing is related to the drainage of subglacial lakes related to the dynamics of the subglacial hydraulic system within SFG and the Antarctic ice sheet. Subglacial lakes upstream of the SFG have been identified with Land Elevation Satellite (ICESat) (Fricker et al., 2016). When the water pressure in these subglacial lakes reaches a critical threshold, the meltwater can escape, leading to a larger discharge at the grounding line of SFG. Dow et al. (2022) proposed that the Foundation Ice Stream (southwest of SFG) system contains a network of extensive channels interconnected with subglacial lakes, providing a plausible pathway for increased discharge resulting from lake drainage, as evidenced by a significant discharge of 24 m^3s^{-1} at the grounding line. Considering the inclusion of lake drainage in the smaller channels at SFG, a maximum discharge of 9 m^3s^{-1} during a lake drainage event is well within the realm of feasibility.

This analysis enables the determination of the precise timing of the arrival of the subglacial runoff freshwater flux at FSE2. By subtracting the travel time (t = 50 days) required for a water mass to travel from the grounding line to the FSE2 location from the starting date of the subglacial event, the discharge timing of these subglacial runoff events at the grounding line can be approximated. Hence, the discharge times at the grounding line of the observed pulses can roughly expected to occur: early November 2015 (starting date unknown,

based on minimum source salinity), mid-February 2016, mid-November 2017, late April 2019, early February 2020, mid-December 2020. By using satellite imagery detection of subglacial lakes, it is now possible to investigate the potential relationship between discharge time and the drainage of subglacial lakes within the ice sheet in future studies. However, it is important to notice that the velocity used in the calculations is the mean current at 1080m. However, this does not consider the change in the direction of the mean current from north to south in the upper layer during the period. The tidal current is also filtered out, which is expected to influence the current velocity greatly

The freshwater flux model obtained in this study may have certain limitations arising from the simplifications made in the calculations. The assumption of a constant basal meltwater flux is not valid for the entire basal meltwater channel. The changes in ice shelf water plume dynamics due to the freshwater input will feed back on the melt rates. Generally, the flux estimates should be considered as a scale estimate rather than an exact quantification. The increased percentages of freshwater content from January 2017 to August 2018 can result from the delayed increasing trend in source salinity between the source water mass of the ISW and the 750 m measurements. The estimation of freshwater content is determined by the fraction between the source water mass and the salinity measured at 750m depth. Because the increasing trend in salinity is later observed in the upper layer, the fraction in Eq.3.4 will be larger, which may explain the increasing freshwater percentage. Although the approximations may overestimate, it is still a good illustration that pulses of increased subglacial runoff flux are occurring and that these pulses coincide with the subglacial runoff pulses observed in the other oceanic properties

5.3 Characterizing Subglacial Runoff Events and the Formation of an Ice Shelf Water Plume

Earlier observations below FRIS show that the background circulation is mainly driven by large-scale density gradients inside the cavity, giving rise to geostrophic currents that follow the topographic contours inside the cavity (Hattermann et al., 2021; Nicholls et al., 2009a), illustrated in Fig. 5.1a. The time series analysis reveals that the characteristic pattern observed during subglacial runoff events interacts with and influences the background flow, potentially altering its dynamics and magnitude. Specifically, the subglacial runoff events exhibit a distinct pattern that can be described in two phases. During the early phase (phase 1), the source water salinity decreases, temperature increases, and southward velocity anomalies are observed in the upper layer. This phase is followed by a second phase (phase 2), where the source water salinity rapidly increases,

temperature decreases, and northward velocity anomalies are present. It is hypothesized that this evolution is caused by distinct subglacial runoff pulses and the formation of an ice shelf water plume generated by these events (Fig.**??**b,c).

During phase 1, the water within the upper layer exhibits lower source salinity and warmer characteristics, indicative of the direct influence of the fresh subglacial runoff (illustrated in Fig.5.1b). The backscatter signal also increases during this phase. Research conducted by Powell (1990); Drews et al. (2017) demonstrated that subglacial discharge is known to transport glacially-eroded sediments, making it highly possible that the observed increased back-scatter signal is a cause of sediments deposited by the glacier. Also, because the signal is delayed with depth, the backscatter signal is not a result of increased ice crystal presence, as ice crystals would ascend, and the signal would be observed from the seafloor towards the surface (Oraltay and Hallett, 1989). This indicates that the increased signal is caused by increased sediments within the subglacial runoff event and that phase 1 is most relevant for transporting sediments. Building upon the findings of Schild et al. (2016), it becomes evident that the increased back-scatter signal can be used as a indicator of a plume resulting from subglacial runoff. During phase 2, there is a transition to colder water masses containing higher source salinity (illustrated in Fig.5.1c). This shift in water properties proposes an increased contribution from basal meltwater, aligning with enhanced basal melting in the deeper regions of the ice shelf. When subglacial runoff enters the ice shelf cavity at the grounding line, a catalytic effect is initiated, facilitating the entrainment of relatively saline ISW (Fig.5.1b) (Jenkins, 2011). Typically confined to the bottom layer of the ice shelf cavity, this less modified ISW exhibits higher salinity and temperature than the stronger modified ISW above. Through the process of entrainment, the less modified ISW is transported to the ocean-ice shelf interface, which will potentially drive melting. This leads to an additional buoyancy input that surpasses the initial buoyancy contribution from the limited volume flux of the subglacial runoff, ultimately accelerating the plume velocity (Fig.5.1c). The upper layer during phase 2 is hypothesized to contain a mixture of the entrained less modified ISW with higher source salinity and the basal meltwater resulting from the plume interactions with the deep ice shelf base, which brings the temperature down and increases the source salinity.

The observed smooth transition between the two phases at FSE2 is consistent with a gradual transition in the driving mechanism of the plume, described by Jenkins (2011). The melting near the grounding line is initially driven by convection caused by the subglacial discharge, leading to the first phase. Subsequently, the plume is initialized and further accelerated by shear-driven melt and the entrainment of less modified ISW. This progression leads to the second phase, where it appears that the subglacial runoff discharge at the grounding line no longer serves as the dominant source of buoyancy. This unique gene-

sis of the plume has not yet been directly observed but is anticipated to have implications for the intensity of basal melting near the grounding line. Understanding these processes is important for assessing ice shelf thinning and land ice discharge (Reese et al., 2018). Detailed modeling will be necessary to fully understand the plume's dynamics and the precise reasons for basal melt pulses following the subglacial runoff pulses.

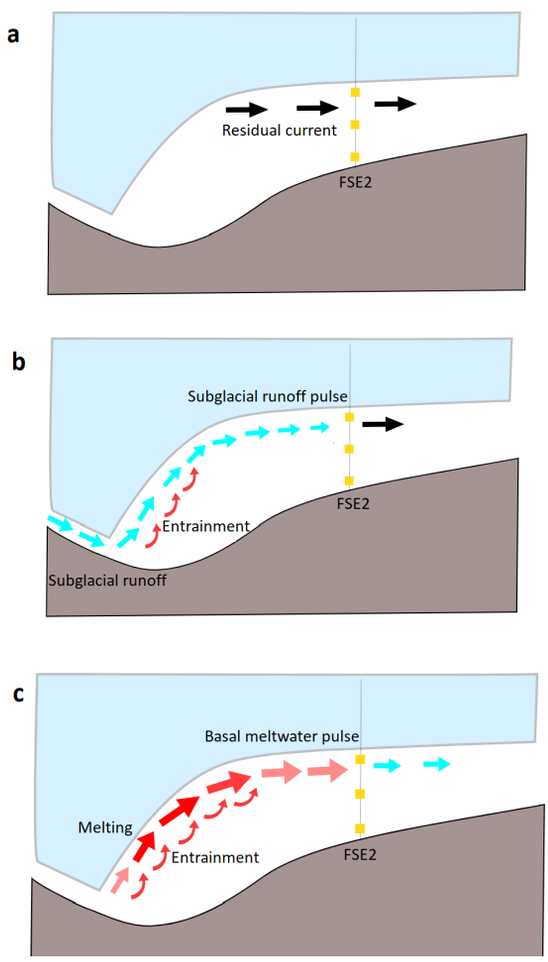

Figure 5.1: Different scenarios of the mean current beneath FIS based on observations at FSE2. (a) illustrate a normal state where the background current dominates the residual current. (b) Show subglacial runoff discharged at the grounding line of SFG, which results in a plume facilitating the entrainment of warmer and more saline water from the deeper parts of the ice shelf cavity, initiating phase 1 of the subglacial runoff event. And (c) shows the evolution of the plume, inducing melting of the ice shelf base and continued entrainment of warmer and more saline water resulting in an altering of the water masses properties within the plume and a larger volume flux, forming phase 2 of the subglacial runoff event.

5.4 Background Current and Local Circulation Variations beneath Filchner Ice Shelf

The current beneath FIS is a superposition of a highly variable tidal current, a slow background current from the west driven by Ronne-HSSW, and local variations in the current (Hattermann et al., 2021; Nicholls et al., 2009a). In the previous analysis in Chapter 5.3, it was discussed that the observed local variations in the upper layer are consistent with an ISW plume triggered from subglacial runoff discharged at the grounding line of SFG. In addition, the analysis of the time series data indicates the existence of variations in the background current, with the runoff events superimposed upon them.

From January 2016 to May 2018, the background current was directed northward in the upper and bottom layers, with higher velocities observed in the bottom layer. In this analysis, the oscillating effects from the tidal current are intentionally removed to focus on assessing the residual flow. Therefore, the northward mean current observed is solely attributed to the residual current, which refers to the background current and anomalies. The mean current in the bottom layer is directed in the northeast and is considered geostrophic. Consequently, the background current from the west, which follows the topography contours, dominates the bottom layer. When considering only the effects of baroclinicity, water with lower density indicates low pressure within the water column. In the Southern hemisphere, the low pressure is to the right of a geostrophic current, indicating lighter water masses to the east of FSE2 for the geostrophic current to flow northward. The east-west horizontal density gradient, combined with the stratified water column leading to an incline in the isopycnals, results in a changing pressure gradient force with depth. Consequently, a vertical velocity shear is observed, decreasing from the bottom toward the surface, following the thermal wind relation ($\frac{\partial v}{\partial z} < 0$). From the thermal wind shear (Eq.2.5a), a wind shear decreasing with height indicates that larger horizontal density differences are found in the bottom layer compared to the upper layer.

During phase 1, which corresponds to the early stage of the subglacial runoff event (as discussed in Chapter 5.3), a vertical velocity shear is observed, decreasing from the bottom towards the ice shelf base ($\frac{\partial v}{\partial z} < 0$). The vertical velocity shear is also observed to rotate counterclockwise, progressing from the bottom toward the ice shelf base. A deflection to the west is observed in the upper layer, illustrated in Fig5.2a. The deflection cannot be explained by the theory of the Ekman spiral in an under-ice boundary layer because the frictional forces from the ice shelf base act in the opposite direction of the mean current. Thus the mean velocity would be expected to have a frictional-induced component down the pressure gradient, influencing the current in the upper

layer to be deflected towards the east (Marshall and Plumb, 2007). Small friction coefficients at the ice base (Holland and Feltham, 2006) may explain the minor importance of the Ekman layer, suggesting that the westward deflection of the velocities at the uppermost current meter is dominated by other effects than boundary layer friction. The underlying reasons for the rotation remain unclear but may be related to ageostrophic convergence/divergence or be associated with the conservation of potential vorticity when there are variations in the thickness of the water column beneath the ice shelf. The height changes can induce the relative vorticity to adjust to uphold the conservation principle. In the Southern Hemisphere, the counterclockwise motion observed can be attributed to negative relative vorticity (Rohli and Vega, 2011), consistent with a decrease in water column height along the flow path. The dominance of the rotating vertical velocity shear within the water column during phase 1, driven by horizontal density variations, proposes that the background current is dominant in driving the flow dynamics during this stage of the subglacial runoff event.

In phase 2 of the subglacial runoff event, the later stage of the plume which contains basal meltwater (as discussed in Chapter 5.3), the mean current in the upper layer undergoes alterations (Fig.5.2c), with the mean current at 750 m shifting towards the northeast and an increase in velocity at 750 m and 840 m. These alterations are consistent with a developed buoyant meltwater plume. If the plume gains enough volume and velocity, it will approach geostrophic balance and ascend under the ice base with a component aligning with the topographic contours (Holland and Feltham, 2006). Hence, the plume gradually dominates the mean current in the upper layer during phase 2, shaping its overall circulation.

Between May 2018 and July 2020, the background current exhibited a southward direction in the upper layer. The change in direction observed in the upper layer can be attributed to variations in the large-scale density structure within the cavity during the transition into the Ronne mode. Notably, the timing of this Ronne mode transition, as documented by Hattermann et al. (2021), aligns with the observed shift in the background flow direction. During this period of dominant Ronne mode, higher source salinity propagates through the cavity from west to east. This increased salinity leads to denser water in the center of the Filchner Trough, thereby contributing to a larger east-west density gradient, which increases the thermal wind shear. This is consistent with an increase of the bottom intensified northward velocities, while the reversal of the flow at the uppermost current meters may be a response to the increased vertical shear through baroclinic adjustments. During this interval, when a subglacial runoff event occurs, the dominant feature within phase 1 is the pronounced vertical velocity shear resulting from the shift to Ronne mode (Fig.5.2b). This proposes that the background current continues to dominate in phase 1, similar to phase

1 during interval 1. During phase 2 of the subglacial runoff event, the genesis of the meltwater event acts on top of the vertical velocity shear observed in phase 1. This interaction between the plume and the background current leads to similar anomalies as those observed in the first interval, however, being superimposed to a different background flow. The meltwater plume opposes the mean current, which now flows from the north, opposing the background thermal wind shear, leading to a weakening of the southward component at the uppermost current meter (Fig.5.2d).

The distinction between phase 1 and phase 2 of the subglacial runoff event in terms of their impact on the current within the upper layer is assumed to be attributed to the structural characteristics of the plume and the degree of entrainment of HSSW into the plume during its ascent. The lower source salinity and warmer temperature within phase 1 indicate that the subglacial discharge has undergone less entrainment of HSSW compared to the plume generated in phase 2. In phase 2, where the plume is more developed, the plume exhibits a higher level of entrainment, resulting in increased basal melting and subsequent input of buoyancy. This accelerates the plume, ultimately becoming geostrophic, thus influencing the circulation patterns in the upper layer.

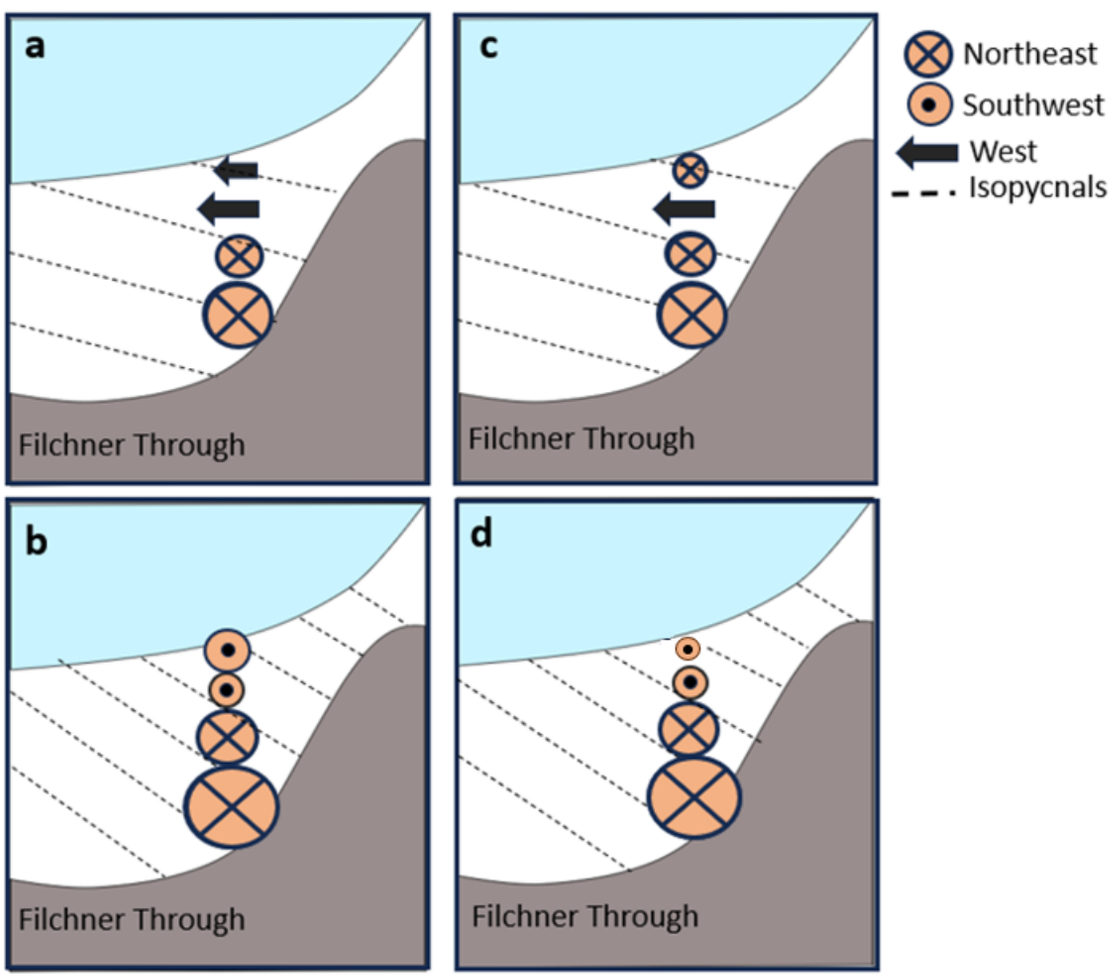

Figure 5.2: Panels (a) and (b) illustrate the vertical velocity shear profiles beneath FIS during phase 1 of the subglacial runoff event. Panels (c) and (d) illustrate the vertical velocity shear profiles during a phase 2 of the subglacial runoff event. The (×) is oriented towards the northeast and the (○) is oriented towards the southwest

5.5 Implications for Ice Shelf Stability

This study has identified subglacial runoff, and for the first time, a time series of runoff from under-ice shelf ocean mooring data has been derived. Furthermore, this study shows that the subglacial runoff induces a basal melt plume, which is observed to alter the residual ocean current in the upper layer, regardless of the direction of the background current.

As demonstrated by Jenkins (2011), the subglacial runoff can act as a trigger, amplifying the formation of a meltwater plume. Discovering a plume with the characteristics of subglacial runoff in front (phase 1) followed by a pulse of basal meltwater (phase 2) 182 km away from the grounding line supports the theory of a subglacial runoff-induced meltwater plume. A larger pulse of subglacial runoff within phase 1 of the subglacial runoff event corresponds to a larger magnitude of phase 2, suggesting that the discharge of subglacial runoff intensifies the melting of the ice shelf base. Consequently, the increased melting caused by subglacial runoff can lead to larger meltwater channels in the ice shelf base (Hofstede et al., 2021a). According to (Millgate et al., 2013) larger meltwater channels can shield other ice shelf areas from the sub-ice shelf plumes. Thus, meltwater channels can reduce average melt rates because they are a topographical focus for the plumes (Dutrieux et al., 2013; Alley et al., 2016). On the other hand, the contribution of subglacial runoff to increased melt rates can have implications for the vulnerability and mass loss of the ice shelf. The enhanced meltwater plume resulting from subglacial runoff can lead to intensified melting, particularly in the deeper regions of the ice shelf. This dynamic melting process is significant for the loss of grounded ice (Reese et al., 2018). The intensification of cold meltwater outflow at FSE2 during phase 2 provides evidence of this process in action. Additionally, the timing of runoff pulses, which exhibit monthly to interannual variability, impacts the temporal variability of melt rates near the grounding line. This aspect is important to consider when interpreting time series of melting from satellite remote sensing (Adusumilli et al., 2020).

As shown in this study, subglacial runoff-induced meltwater plume impacts the current in the upper layer. In the case of larger meltwater channels, the plumes are likely to exhibit a larger volume flux of meltwater, potentially dominating the flow in the upper layer over a longer period. The upper layer will also be fresher due to more basal meltwater and experience more vertical mixing of heat, which can change the stratification of the water column and induce higher melt rates. Changes in stratification in one area can induce horizontal density gradients, impacting the baroclinic geostrophic current beneath the ice shelf.

As climate change continues to affect Antarctica, the impact of subglacial runoff

may evolve. With rising air temperatures, more surface meltwater is likely to accumulate in basins within the ice sheet and eventually reach the ice sheet base, increasing subglacial discharge at the grounding line (Dow et al., 2022). It is possible that the larger subglacial runoff pulses, which are currently not seasonal, could become seasonal in the future. This is similar to what is observed in glaciers in Greenland (Washam et al., 2019). Increasing subglacial discharge at the grounding line will lead to increased formation of ISW plumes beneath FIS, hence a thinning of the ice shelf. Furthermore, reduced buttressing to the ice sheet can cause ice streams to accelerate, resulting in more frictional glacial basal melt (Pritchard et al., 2012). This phenomenon is not limited to FIS but is expected to occur across all ice shelves in Antarctica. Incorporating subglacial runoff into ice sheet models could improve the understanding of ice sheet dynamics and help to make more accurate future predictions of ice sheet stability.

/6

Summary

This study has expanded our knowledge of the general circulation beneath FIS. Previous studies show that the current in this region is a combination of various components, including a highly variable tidal current, a slow background current from the west driven by Ronne-HSSW, and local variations (Hattermann et al., 2021; Nicholls et al., 2009a). This study shows that these local variations observed beneath FIS result from an ISW plume caused by subglacial runoff discharged at the grounding line of SFG.

This study shows that freshwater from subglacial runoff spreads over the shallower regions of the western and eastern flanks beneath FIS. The observed distribution is consistent with the buoyancy-driven ascent of subglacial runoff along the inclined ice shelf base and the effects of the Earth's rotation, causing it to flow with constant topographic contours. The stratification in source salinity throughout the time series suggests a consistent presence of subglacial runoff at FSE2, which can be caused by a constant discharge of subglacial runoff due to geothermal heating or melting from ice sliding over the bedrock. The occurrence of six larger events of subglacial runoff in the upper layers is assumed to be due to the drainage of subglacial lakes, which contain accumulated glacial basal meltwater within the ice sheet. A time series of the subglacial runoff have been derived from the under-ice shelf ocean mooring data for the first time. The time series reveals that the pulses of subglacial runoff are not seasonal and exhibit multimonth to interannual variability.

The analysis reveals a notable pattern within the subglacial runoff event: every

larger pulse of subglacial runoff (phase 1) is followed by a larger pulse of basal meltwater (phase 2), indicating increased melting in the deeper regions of the ice shelf. When the subglacial runoff is discharged at the grounding line, it generates a buoyant plume that rises along the ice shelf base, entraining warmer water masses and facilitating basal melting at the ocean-ice shelf interface. The presence of subsequent pulses of basal meltwater has been observed to alter the mean current within the mixed layer, influencing the background thermal wind shear within the background current. This suggests that the pulses of basal meltwater influence the flow dynamics, leading to changes in the current patterns located 182 km upstream of the grounding line. The results further deepen our understanding of the intricate interactions between subglacial processes, basal melting, and ocean current beneath FIS. It highlights the role of subglacial runoff in driving increased melt rates, possibly impacting the vulnerability and mass loss of the ice shelves.

As climate change progresses, the influence of subglacial runoff may evolve. Rising air temperatures are expected to increase surface meltwater accumulation, which can lead to greater subglacial discharge at the grounding line, as observed in Greenland (Washam et al., 2019). This could result in larger, possibly seasonal, subglacial runoff pulses and more pronounced basal meltwater plume formation beneath FIS. Subglacial runoff at grounding lines is not limited to FIS but is anticipated to occur across all ice shelves surrounding the Antarctic ice sheet. This study shows the importance of incorporating subglacial runoff into ice sheet models to improve our understanding of ice sheet dynamics and enhance future ice sheet stability predictions.

6.1 Future Work

To further investigate the effects of subglacial runoff, it would be recommended to incorporate subglacial runoff flux into various models. Integrating subglacial runoff into an ocean circulation model, specifically applied to the ocean cavity beneath the FIS, can achieve a more comprehensive understanding of the effects on the larger circulation pattern beneath the ice shelf. This approach will provide valuable insights beyond examining a single point, such as FSE2, enabling a more detailed assessment of subglacial runoff's influence on the overall circulation. In addition, examining the impacts of subglacial runoff from the Foundation ice stream on the ocean circulation beneath FIS, situated southwest of SFG, would be of interest. The Foundation ice stream is expected to exhibit an even greater magnitude of subglacial discharge at the grounding line (Dow et al., 2022).

To better comprehend the dynamics of the observed ISW pattern, where two

different phases are detected at FSE2, it would be recommended to conduct further investigations into the plume dynamics generated by the subglacial discharge. The models should be run with different magnitudes of subglacial runoff flux. This approach will explore how larger discharges, which may be experienced in the future, impact melt rates and circulation patterns. By quantifying the relationship between subglacial flux magnitude and its consequences, valuable insights can be gained to assess the potential implications of future scenarios.

It would be interesting to investigate the missing data in the current meter dataset to gain a complete time series from 2015-2023 for all parameters. Furthermore, an investigation should be conducted to determine whether the occurrence of larger subglacial pulses aligns with instances of lake drainage within the ice sheet. Leveraging satellite imagery, we now possess an approximation of the timing of discharge at the grounding line, making it possible to investigate this relationship.

Lastly, it is important to prioritize monitoring of ice shelves. In light of the evident effects of the increased melting of ice shelves in Antarctica Paolo et al. (2015); Jenkins et al. (2018); Adusumilli et al. (2020), continuous monitoring of the ice shelves is imperative. These ice shelves greatly impact the Antarctic Ice Sheet mass balance and contribute to bottom water formation. By ensuring ongoing monitoring, we can gather valuable data to enhance our understanding of these critical processes and their broader implications.

Bibliography

Adusumilli, S., Fricker, H. A., Medley, B., Padman, L., and Siegfried, M. R. (2020). Interannual variations in meltwater input to the southern ocean from antarctic ice shelves. *Nature Geoscience*, 13(9):616–620.

Alfred Wegener Institute (2023). The filchner ice shelf project (fisp) - oceanography. `https://www.awi.de/en/science/climate-sciences/physical-oceanography/projects/fisp.htm`. online; accessed 19-January-2023.

Alley, K. E., Scambos, T. A., Siegfried, M. R., and Fricker, H. A. (2016). Impacts of warm water on antarctic ice shelf stability through basal channel formation. *Nature Geoscience*, 9(4):290–293.

Alley, R. (2011). K.m. cuffey and w.s.b. paterson. 2010. the physics of glaciers. fourth edition. amsterdam, etc., academic press. 704pp. isbn-10: 0-123694-61-2, isbn-13: 978-0-123-69461-4, hardback, £60.99/€71.95/us99.95. *Journal of Glaciology*, 57(202) : 383˘384.

Bennett, M. R. (2003). Ice streams as the arteries of an ice sheet: their mechanics, stability and significance. *Earth-Science Reviews*, 61(3):309–339.

Chandler, D. M., Wadham, J. L., Lis, G. P., Cowton, T., Sole, A., Bartholomew, I., Telling, J., Nienow, P., Bagshaw, E. B., Mair, D., Vinen, S., and Hubbard, A. (2013). Evolution of the subglacial drainage system beneath the greenland ice sheet revealed by tracers. *Nature Geoscience*, 6(3):195–198.

Cheng, Y., Xia, M., Qiao, G., Lv, D., Li, Y., and Hai, G. (2021). Imminent calving accelerated by increased instability of the brunt ice shelf, in response to climate warming. *Earth and Planetary Science Letters*, 572:117132.

Depoorter, M. A., Bamber, J. L., Griggs, J. A., Lenaerts, J. T. M., Ligtenberg, S. R. M., van den Broeke, M. R., and Moholdt, G. (2013). Calving fluxes and basal melt rates of antarctic ice shelves. *Nature*, 502(7469):89–92.

Dow, C. F., Ross, N., Jeofry, H., Siu, K., and Siegert, M. J. (2022). Antarctic basal environment shaped by high-pressure flow through a subglacial river system. *Nature Geoscience*, 15(11):892–898.

Dow, C. F., Werder, M. A., Babonis, G., Nowicki, S., Walker, R. T., Csatho, B., and Morlighem, M. (2018). Dynamics of active subglacial lakes in recovery ice stream. *Journal of Geophysical Research: Earth Surface*, 123(4):837–850.

Dow, C. F., Werder, M. A., Nowicki, S., and Walker, R. T. (2016). Modeling antarctic subglacial lake filling and drainage cycles. *The Cryosphere*, 10(4):1381–1393.

Drentea, C. (2010). *Modern Communications Receiver Design and Technology*. Artech House intelligence and information operations series. Artech House, 685 Canton Street, Norwood, USA. pp 393-395.

Drews, R. (2015). Evolution of ice-shelf channels in antarctic ice shelves. *The Cryosphere*, 9(3):1169–1181.

Drews, R., Pattyn, F., Hewitt, I. J., Ng, F. S. L., Berger, S., Matsuoka, K., Helm, V., Bergeot, N., Favier, L., and Neckel, N. (2017). Actively evolving subglacial conduits and eskers initiate ice shelf channels at an antarctic grounding line. *Nature Communications*, 8(1):15228.

Durst, F., Launder, B., Schmidt, F., and Whitelaw, J. (2012). *Turbulent Shear Flows I: Selected Papers from the First International Symposium on Turbulent Shear Flows, The Pennsylvania State University, University Park, Pennsylvania, USA, April 18–20, 1977*. Springer Berlin Heidelberg, Berlin, Germany. pp 20-30.

Dutrieux, P., Vaughan, D. G., Corr, H. F. J., Jenkins, A., Holland, P. R., Joughin, I., and Fleming, A. H. (2013). Pine island glacier ice shelf melt distributed at kilometre scales. *The Cryosphere*, 7(5):1543–1555.

Fofonoff, N. P. and Millard Jr, R. C. (1983). *Algorithms for the computation of fundamental properties of seawater*. Number 44 in UNESCO Technical Papers in Marine Sciences. UNESCO, Paris, France. pp 53.

Fountain, A. G. and Walder, J. S. (1998). Water flow through temperate glaciers. *Reviews of Geophysics*, 36(3):299–328.

Fricker, H. A., Scambos, T., Bindschadler, R., and Padman, L. (2007). An active subglacial water system in west antarctica mapped from space. *Science*, 315(5818):1544–1548.

Fricker, H. A., Siegfried, M. R., Carter, S. P., and Scambos, T. A. (2016). A decade of

progress in observing and modelling antarctic subglacial water systems. *Philosophical Transactions of the Royal Society A: Mathematical, Physical and Engineering Sciences*, 374(2059):20140294.

Gade, H. G. (1979). Melting of ice in sea water: A primitive model with application to the antarctic ice shelf and icebergs. *J. Phys. Oceanogr.*, 9:189–198.

Goldberg, D., Holland, D., and Schoof, C. (2009). Grounding line movement and ice shelf buttressing in marine ice sheets. *Journal of Geophysical Research: Earth Surface*, 114(F4).

Greve, R. and Blatter, H. (2016). Comparison of thermodynamics solvers in the polythermal ice sheet model sicopolis. *Polar Science*, 10(1):11–23.

Hagg, W. (2022). *Glaciology and Glacial Geomorphology*. Springer Berlin Heidelberg, Heidelberger Platz 3, 14197 Berlin, Germany. pp 23.

Haid, V. and Timmermann, R. (2013). Simulated heat flux and sea ice production at coastal polynyas in the southwestern weddell sea. *Journal of Geophysical Research: Oceans*, 118(5):2640–2652.

Hattermann, T., Nicholls, K. W., Hellmer, H. H., Davis, P. E. D., Janout, M. A., Østerhus, S., Schlosser, E., Rohardt, G., and Kanzow, T. (2021). Observed interannual changes beneath filchner-ronne ice shelf linked to large-scale atmospheric circulation. *Nature Communications*, 12(1):2961.

Hofstede, C., Beyer, S., Corr, H., Eisen, O., Hattermann, T., Helm, V., Neckel, N., Smith, E. C., Steinhage, D., Zeising, O., and Humbert, A. (2021a). Evidence for a grounding line fan at the onset of a basal channel under the ice shelf of support force glacier, antarctica, revealed by reflection seismics. *The Cryosphere*, 15(3):1517–1535.

Hofstede, C., Beyer, S., Corr, H., Eisen, O., Hattermann, T., Helm, V., Neckel, N., Smith, E. C., Steinhage, D., Zeising, O., and Humbert, A. (2021b). Evidence for a grounding line fan at the onset of a basal channel under the ice shelf of support force glacier, antarctica, revealed by reflection seismics. *The Cryosphere*, 15(3):1517–1535.

Holland, P. R. and Feltham, D. L. (2006). The effects of rotation and ice shelf topography on frazil-laden ice shelf water plumes. *Journal of Physical Oceanography*, 36(12):2312 – 2327.

Huhn, O., Hattermann, T., Davis, P. E. D., Dunker, E., Hellmer, H. H., Nicholls, K. W., Østerhus, S., Rhein, M., Schröder, M., and Sültenfuß, J. (2018). Basal melt and

freezing rates from first noble gas samples beneath an ice shelf. *Geophysical Research Letters*, 45(16):8455–8461.

Janout, M. A., Hellmer, H. H., Hattermann, T., Huhn, O., Sültenfuss, J., Østerhus, S., Stulic, L., Ryan, S., Schröder, M., and Kanzow, T. (2021). Fris revisited in 2018: On the circulation and water masses at the filchner and ronne ice shelves in the southern weddell sea. *Journal of Geophysical Research: Oceans*, 126(6):e2021JC017269. e2021JC017269 2021JC017269.

Jenkins, A. (2011). Convection-driven melting near the grounding lines of ice shelves and tidewater glaciers. *Journal of Physical Oceanography*, 41(12):2279 – 2294.

Jenkins, A., Shoosmith, D., Dutrieux, P., Jacobs, S., Kim, T. W., Lee, S. H., Ha, H. K., and Stammerjohn, S. (2018). West antarctic ice sheet retreat in the amundsen sea driven by decadal oceanic variability. *Nature Geoscience*, 11(10):733–738.

Jezek, K. C. (1999). Glaciological properties of the antarctic ice sheet from radarsat-1 synthetic aperture radar imagery. *Annals of Glaciology*, 29:286–290.

Joughin, I. and Vaughan, D. G. (2004). Marine ice beneath the filchner–ronne ice shelf, antarctica: a comparison of estimated thickness distributions. *Annals of Glaciology*, 39:511–517.

Kerr, R. C. (1994). Dissolving driven by vigorous compositional convection. *Journal of Fluid Mechanics*, 280:287–302.

Kerr, R. C. and McConnochie, C. D. (2015). Dissolution of a vertical solid surface by turbulent compositional convection. *Journal of Fluid Mechanics*, 765:211–228.

Klinger, B. and Haine, T. (2019). *Ocean Circulation in Three Dimensions*. Cambridge University Press, Cambridge CB2 8BS, United Kingdom.

Knight, P. G. (1999). *Glaciers*. Stanley Thomes (Publishers) Ltd, Ellenborough House, Wellington Street, CHELTENHAM, GL501YW, United Kingdom. pp 53 - 104.

Lambrecht, A., Sandhäger, H., Vaughan, D., and Mayer, C. (2007). New ice thickness maps of filchner–ronne ice shelf, antarctica, with specific focus on grounding lines and marine ice. *Antarctic Science*, 19(4):521–532.

Lilly, Jonathan (2023). Time-series: Course files for ocean/atmosphere time series analysis. `https://github.com/jonathanlilly/time-series`. online; accessed 23-February-2023.

MacAyeal, D. R. (1984). Numerical simulations of the ross sea tides. *Journal of Geophysical Research: Oceans*, 89(C1):607–615.

Makinson, K. and Nicholls, K. W. (1999). Modeling tidal currents beneath filchner-ronne ice shelf and on the adjacent continental shelf: Their effect on mixing and transport. *Journal of Geophysical Research: Oceans*, 104(C6):13449–13465.

Malyarenko, A., Wells, A. J., Langhorne, P. J., Robinson, N. J., Williams, M. J., and Nicholls, K. W. (2020). A synthesis of thermodynamic ablation at ice–ocean interfaces from theory, observations and models. *Ocean Modelling*, 154:101692.

Marshall, J. and Plumb, R. (2007). *Atmosphere, Ocean and Climate Dynamics: An Introductory Text*. International Geophysics. Elsevier Science, 84 Theobald's Road, London WC1X 8RR, United Kingdom. pp 100-150.

Mather, P. (2004). *Computer Processing of Remotely-Sensed Images: An Introduction*. John Wiley & Sons Ltd, West Sussex, England, 3 edition. pp 145 - 155.

Matsuoka, K., Hindmarsh, R. C., Moholdt, G., Bentley, M. J., Pritchard, H. D., Brown, J., Conway, H., Drews, R., Durand, G., Goldberg, D., Hattermann, T., Kingslake, J., Lenaerts, J. T., Martín, C., Mulvaney, R., Nicholls, K. W., Pattyn, F., Ross, N., Scambos, T., and Whitehouse, P. L. (2015). Antarctic ice rises and rumples: Their properties and significance for ice-sheet dynamics and evolution. *Earth-Science Reviews*, 150:724–745.

McDougall, T., Feistel, R., and Pawlowicz, R. (2013). *Ocean Circulation and Climate: Chapter 6. Thermodynamics of Seawater*. International Geophysics. Elsevier Science, Amsterdam, Netherlands. pp 10-50.

Millero, F. (1978). Freezing point of seawater. *Eighth Report of the Joint Panel on Oceanographic Tables and Standards*, 28:29–31.

Millgate, T., Holland, P. R., Jenkins, A., and Johnson, H. L. (2013). The effect of basal channels on oceanic ice-shelf melting. *Journal of Geophysical Research: Oceans*, 118(12):6951–6964.

Mitchell, P. (2022). *Experimental Design and Statistical Analysis for Pharmacology and the Biomedical Sciences*. Wiley, 9600 Garsington Road, Oxford, United Kingdom. pp 100-155.

Motyka, R. J., Hunter, L., Echelmeyer, K. A., and Connor, C. (2003). Submarine melting at the terminus of a temperate tidewater glacier, leconte glacier, alaska, u.s.a. *Annals of Glaciology*, 36:57–65.

Nicholls, K. W., Makinson, K., and Østerhus, S. (2004). Circulation and water masses beneath the northern ronne ice shelf, antarctica. *Journal of Geophysical Research: Oceans*, 109(C12).

Nicholls, K. W., Østerhus, S., Makinson, K., Gammelsrød, T., and Fahrbach, E. (2009a). Ice-ocean processes over the continental shelf of the southern weddell sea, antarctica: A review. *Reviews of Geophysics*, 47(3).

Nicholls, K. W., Østerhus, S., Makinson, K., Gammelsrød, T., and Fahrbach, E. (2009b). Ice-ocean processes over the continental shelf of the southern weddell sea, antarctica: A review. *Reviews of Geophysics*, 47(3).

Nicholls, K. W., Østerhus, S., Makinson, K., and Johnson, M. R. (2001). Oceanographic conditions south of berkner island, beneath filchner-ronne ice shelf, antarctica. *Journal of Geophysical Research: Oceans*, 106(C6):11481–11492.

Norsk Polarinstitutt (2023). Quantarctica. `https://www.npolar.no/quantarctica/#toggle-id-1`. online; accessed 13-June-2023.

Oppenheimer, M. (1998). Global warming and the stability of the west antarctic ice sheet. *Nature*, 393(6683):325–332.

Oraltay, R. and Hallett, J. (1989). Evaporation and melting of ice crystals: A laboratory study. *Atmospheric Research*, 24(1):169–189.

Orsi, A., Johnson, G., and Bullister, J. (1999). Circulation, mixing, and production of antarctic bottom water. *Progress in Oceanography*, 43(1):55–109.

Orsi, A. H. and Wiederwohl, C. L. (2009). A recount of ross sea waters. *Deep Sea Research Part II: Topical Studies in Oceanography*, 56(13):778–795. Southern Ocean Shelf Slope Exchange.

Paolo, F. S., Fricker, H. A., and Padman, L. (2015). Volume loss from antarctic ice shelves is accelerating. *Science*, 348(6232):327–331.

Paterson, W. S. B. (1981). *Physics of glaciers*. Pergamon Press, Oxford, England. pp 5-90.

Pattyn, F. (2010). Antarctic subglacial conditions inferred from a hybrid ice sheet/ice stream model. *Earth and Planetary Science Letters*, 295:451–461.

Pickard, G. and Emery, W. (1990). *Descriptive Physical Oceanography: An Introduction*. Elsevier Science, Oxford, England. pp 92-95.

Powell, R. D. (1990). Glacimarine processes at grounding-line fans and their growth to ice-contact deltas. *Geological Society, London, Special Publications*, 53:53 – 73.

Pritchard, H. D., Ligtenberg, S. R. M., Fricker, H. A., Vaughan, D. G., van den Broeke, M. R., and Padman, L. (2012). Antarctic ice-sheet loss driven by basal melting of ice shelves. *Nature*, 484(7395):502–505.

Reese, R., Gudmundsson, G., Levermann, A., and Winkelmann, R. (2018). The far reach of ice-shelf thinning in antarctica. *Nature Climate Change*, 8.

Rignot, E., Casassa, G., Gogineni, P., Krabill, W., Rivera, A., and Thomas, R. (2004). Accelerated ice discharge from the antarctic peninsula following the collapse of larsen b ice shelf. *Geophysical Research Letters*, 31(18).

Rohli, R. and Vega, A. (2011). *Climatology*. Jones & Bartlett Learning, Barb House, London W67PA, United Kingdom. pp 139.

Rossant, C. (2018). *IPython Interactive Computing and Visualization Cookbook: Over 100 hands-on recipes to sharpen your skills in high-performance numerical computing and data science in the Jupyter Notebook, 2nd Edition*. Packt Publishing, 35 Livery Place, Birmingham, England. pp 145 - 150.

Satoh, M. (2004). *Atmospheric Circulation Dynamics and Circulation Models*. Environmental Sciences. Praxis Publishing Ltd, Chichester, UK. pp 56.

Schild, K. M., Hawley, R. L., and Morriss, B. F. (2016). Subglacial hydrology at rink isbræ, west greenland inferred from sediment plume appearance. *Annals of Glaciology*, 57(72):118–127.

Schoof, C. (2007). Ice sheet grounding line dynamics: Steady states, stability, and hysteresis. *Journal of Geophysical Research: Earth Surface*, 112(F3).

Shepherd, A., Ivins, E., Rignot, E., Smith, B., van den Broeke, M., Velicogna, I., Whitehouse, P., Briggs, K., Joughin, I., Krinner, G., Nowicki, S., Payne, T., Scambos, T., Schlegel, N., A, G., Agosta, C., Ahlstrøm, A., Babonis, G., Barletta, V., Blazquez, A., Bonin, J., Csatho, B., Cullather, R., Felikson, D., Fettweis, X., Forsberg, R., Gallee, H., Gardner, A., Gilbert, L., Groh, A., Gunter, B., Hanna, E., Harig, C., Helm, V., Horvath, A., Horwath, M., Khan, S., Kjeldsen, K. K., Konrad, H., Langen, P., Lecavalier, B., Loomis, B., Luthcke, S., McMillan, M., Melini, D., Mernild, S., Mohajerani, Y., Moore, P., Mouginot, J., Moyano, G., Muir, A., Nagler, T., Nield, G., Nilsson, J., Noel, B., Otosaka, I., Pattle, M. E., Peltier, W. R., Pie, N., Rietbroek, R., Rott, H., Sandberg-Sørensen, L., Sasgen, I., Save, H., Scheuchl, B., Schrama, E., Schröder, L., Seo, K.-W., Simonsen, S., Slater, T., Spada, G.,

Sutterley, T., Talpe, M., Tarasov, L., van de Berg, W. J., van der Wal, W., van Wessem, M., Vishwakarma, B. D., Wiese, D., Wouters, B., and The IMBIE team (2018). Mass balance of the antarctic ice sheet from 1992 to 2017. *Nature*, 558(7709):219–222.

Shroder, J., Haeberli, W., and Whiteman, C. (2021). *Snow and Ice-Related Hazards, Risks, and Disasters*. Elsevier Science, The Boulevard, United Kingdom. pp 479.

Siegert, M. J., Carter, S., Tabacco, I., Popov, S., and Blankenship, D. D. (2005). A revised inventory of antarctic subglacial lakes. *Antarctic Science*, 17(3):453–460.

Soulsby, R. (1997). *Dynamics of marine sands*. T. Telford London, UK, London, England. pp 40-50.

Stearns, L. A., Smith, B. E., and Hamilton, G. S. (2008). Increased flow speed on a large east antarctic outlet glacier caused by subglacial floods. *Nature Geoscience*, 1(12):827–831.

Stokes, C. R. and Clark, C. D. (1999). Geomorphological criteria for identifying pleistocene ice streams. *Annals of Glaciology*, 28:67–74.

Tabacco, I. E., Cianfarra, P., Forieri, A., Salvini, F., and Zirizotti, A. (2006). Physiography and tectonic setting of the subglacial lake district between Vostok and Belgica subglacial highlands (Antarctica). *Geophysical Journal International*, 165(3):1029–1040.

Talley, L. (2011). *Descriptive Physical Oceanography: An Introduction*. Elsevier Science, 32 Jamestown Road, London NW1 7BY, UK. 50-250.

Thøgersen, K., Gilbert, A., Schuler, T. V., and Malthe-Sørenssen, A. (2019). Rate-and-state friction explains glacier surge propagation. *Nature Communications*, 10(1):2823.

Washam, P., Nicholls, K. W., Münchow, A., and Padman, L. (2019). Summer surface melt thins petermann gletscher ice shelf by enhancing channelized basal melt. *Journal of Glaciology*, 65(252):662–674.

Woods, A. W. (1992). Melting and dissolving. *Journal of Fluid Mechanics*, 239:429–448.

Wright, A. and Siegert, M. (2012). A fourth inventory of antarctic subglacial lakes. *Antarctic Science*, 24(6):659–664.

Wåhlin, A. K., Yuan, X., Björk, G., and Nohr, C. (2010). Inflow of warm circumpolar

deep water in the central amundsen shelf. *Journal of Physical Oceanography*, 40(6):1427 – 1434.

Zeising, O., Steinhage, D., Nicholls, K. W., Corr, H. F. J., Stewart, C. L., and Humbert, A. (2022). Basal melt of the southern filchner ice shelf, antarctica. *The Cryosphere*, 16(4):1469–1482.

7

Appendix

7.1 Hanning Window

The Hanning window is a type of window function commonly used in signal processing and data analysis to avoid leakage at the boundaries at the windows. The Hanning Window is expressed as

$$w(n) = 0.5\left(1 - \cos\left(\frac{2\pi n}{N-1}\right)\right) \tag{7.1}$$

Where the value of the window at a specific index n is represented by w(n), and N indicates the total number of samples contained within the window (Drentea, 2010).

7.2 Variance, Covariance, and Stander deviation

The variance of a variable quantifies the average spread or dispersion of its data points around the mean. A higher variance indicates a greater spread or variability in the data, while a lower variance suggests a more concentrated or less variable distribution (Mitchell, 2022). The variance of a variable x is calculated using the following formula:

$$\mathrm{Var}(x) = \frac{1}{n}\sum_{i=1}^{n}(x_i - \mu)^2 \tag{7.2}$$

Where x represents the variable (in this case, either u or v), n is the total number of data points, x_i represents each data point of variable x and μ represents the mean of the data points (Mitchell, 2022).

Covariance measures the linear relationship between two variables. It quantifies how changes in one variable correspond to changes in the other (Mitchell, 2022). A positive covariance indicates that u and v tend to vary in the same direction, while a negative covariance suggests they vary in opposite directions. The covariance between two variables X and Y is calculated using the following formula:

$$\text{cov}(X, Y) = \frac{1}{n} \sum_{i=1}^{n} (x_i - \mu_X)(y_i - \mu_Y) \tag{7.3}$$

Where X and Y represent the variables (u and v in this case), x_i and y_i represent the individual data points of variables X and Y. μ_X and μ_Y represent the respective means of X and Y (Mitchell, 2022).

Standard deviation is a statistical measure that quantifies the variability of data points from the mean. A larger standard deviation indicates a greater amount of variability or dispersion from the mean. Conversely, a smaller standard deviation suggests that the values are closer together, with less variability around the mean. The stander deviation is expressed as the square root of the variance:

$$\sqrt{\left(\frac{1}{n} \sum_{i=1}^{N} (x_i - \mu)^2\right)} \tag{7.4}$$

Where the variable is expressed in Eq.7.2 (Mitchell, 2022).

7.3 Covariance ellipse

The variance ellipse is a graphical representation used to describe the uncertainty or variability associated with velocity anomalies, which provides information about the magnitude and direction of variability in the flow field (Mather, 2004). The derivation of the variance ellipse is based on the work from Lilly, Jonathan (2023). To construct the variance ellipse, the major and minor axes, as well as the orientation, have to be determined. This is derived from the eigenvalues and eigenvectors from the Covariance matrix. The covariance matrix, denoted as C, is a mathematical representation that describes the relationship between the covariances and variances of variables in a dataset, in this case the velocity component vectors u and v. It can be expressed as:

$$C = \begin{bmatrix} \text{var}(u) & \text{cov}(u, v) \\ \text{cov}(u, v) & \text{var}(v) \end{bmatrix} \tag{7.5}$$

In this context, var(u) and var(v) represent the variances of the velocity component vectors u and v, cov(u, v) is the covariance of the u and v vectors.
The semi-major axis (a) represents the length of the longest axis and is calculated as the square root of the first eigenvalue (λ_1) of the covariance matrix:

$$a = \sqrt{\lambda_1} \tag{7.6}$$

Similarly, the semi-minor axis (b) corresponds to the length of the shortest axis and is calculated as the square root of the second eigenvalue (λ_2) of the covariance matrix:

$$b = \sqrt{\lambda_2} \tag{7.7}$$

The eigenvalues is further obtained from deriving the determinant of $|C - \lambda I| = 0$, where C is the covariance matrix, I is the identity matrix and λ is the eigenvalues. Solving for the eigenvalues, the semi-minor and semi-major axis can be expressed as:

$$a, b = \sqrt{\frac{\mathrm{Tr}(C)}{2} \pm \frac{\sqrt{\mathrm{Tr}(C)^2 - 4 \times \mathrm{Det}(C)}}{2}} \tag{7.8}$$

Where Tr(C) represents the trace of the covariance matrix, which captures the total variability, and Det(C) represents the determinant of the covariance matrix, reflecting the overall spread or variability of the data distribution.

The orientation (θ) of the variance ellipse is expressed in terms of the eigenvectors, $(C - \lambda I)e = 0$, where e represents the eigenvector. It represents the angle between the eigenvector corresponding to the semi-major axis and the x-axis. For two-dimensional data, it can be calculated as:

$$\theta = \frac{1}{2} \arctan\left(\frac{2\mathrm{cov}(u, v)}{\mathrm{var}(u) - \mathrm{var}(v)}\right) \tag{7.9}$$

The variance ellipse could be expressed as a collection of complex numbers that describe the boundary or outer edge of an ellipse, i terms of the semi axes (a,b) and orientation (θ):

$$z = \exp^{j\theta}(a\cos(\phi) - jb\sin(\phi)) \tag{7.10}$$

Where ϕ represents an array of angles ranging from 0 to 2π.